Aerotecnica Missili & Spazio (2025) 104:387–414
https://doi.org/10.1007/s42496-024-00240-6

RESEARCH

# Angle of Attack Effects on the Induced Structural Loads of a Weapons Bay

**David Bacci**[1] · **Alistair J. Saddington**[2]

Received: 1 May 2024 / Revised: 7 November 2024 / Accepted: 11 November 2024 / Published online: 3 December 2024


**Abstract**
Aero-acoustic analysis was conducted on a weapons bay numerical model with doors, incorporating radar cross section reduction features. The effect of the angle of attack on the aero-acoustic response of the cavity was analysed at Mach numbers of 0.85 and 1.20. It was found that incidence influenced both mean-flow features and acoustic response. Further, linear and angular accelerations induced by the flow on the bay doors revealed potential adverse fluid–structure coupling when the results were compared with modal analysis. Again, the angle of attack did influence the aeroacoustic effects on the cavity door structure.

**Keywords** Weapons-Bay · Cavity-flow · Scale-adaptive-simulations · Modal-analysis

**List of Symbols**

| | |
|---|---|
| $f$ | Frequency [Hz] |
| $f_s$ | Sampling frequency [Hz] |
| $f_r$ | Frequency resolution [Hz] |
| $\gamma$ | Ratio of specific heats for air |
| $\omega$ | Angular velocity [rad/s] |
| $\dot{\omega}$ | Angular acceleration [rad/s$^2$] |
| $M$ | Mach number |
| $M_n$ | $n_{th}$ Structural mode |
| $R_n$ | $n_{th}$ Acoustic resonant mode |
| $\mathrm{RH}_n$ | $n_{th}$ Rossiter-Heller theory predicted mode |
| $St$ | Strouhal number $(= f \cdot D/U)$ |
| $U$ | Air speed |
| $t_c$ | Convective time $(= L/U_\infty)$ |
| $\overline{x}$ | Time-averaged value of the discrete-time series $x_n$ $(\sum_{j=1}^{N} x_j/N)$ |
| $\widehat{X}$ | Discrete Fourier transform of the variable $x$ |
| $X^*$ | Complex conjugate of the variable $X$ |
| $\mu_x$ | Mean of variable $x$ |
| $\sigma_x$ | Root mean square of variable $x$ |
| $\sigma_s$ | Stress [Pa] |
| $p$ | Air pressure |
| $q$ | Dynamic pressure |
| $\delta_0$ | Boundary layer thickness at cavity leading edge |
| $\rho$ | Air density |
| $L$ | Cavity length |
| $W$ | Cavity width |
| $D$ | Cavity dept |
| $\vec{u}$ | Displacement vector of structure [m] |
| $\vec{\theta}$ | Rotation vector of structure [rad] |
| $m$ | Mass [kg] |
| $\overleftrightarrow{I}$ | Inertial tensor [kgm$^2$] |
| $a$ | Acceleration [m/s$^2$] |
| $\alpha$ | Angle of attack [deg] |
| $\beta$ | Angle of sideslip [deg] |
| $k$ | Turbulent kinetic energy $\left[m^2/s^2\right]$ |
| $\omega$ | Specific dissipation rate $\left[1/s\right]$ |
| $E$ | Young's modulus [Pa] |
| $\epsilon$ | Entity of deformation of modal analysis $\left(= \sigma_s \vec{u} / E\Delta \vec{u}\right)$ |

**Subscripts**

| | |
|---|---|
| $\infty$ | Free-stream conditions |

✉ David Bacci
david.bacci@eng.ox.ac.uk

[1] Oxford Thermofluids Institute, Department of Engineering Science, University of Oxford, Oxford OX2 0ES, UK

[2] Aeromechanical Systems Group, Centre for Defence Engineering, Cranfield University, Shrivenham SN6 8LA, UK

## 1 Introduction

Design requirements for modern combat aircraft are strongly influenced by the requirement to reduce the radar signature. This implies that weapons must be carried inside

the airframe, instead of being suspended on the wing and fuselage. Whilst this solution offers advantages in terms of aerodynamic drag reduction (especially at transonic and supersonic speeds), other issues are generated because, during the weapon release procedure when the bay's doors are opened and the cavity is exposed to high-speed flow, an intense acoustic field is developed capable of damaging the airframe and the payload. Additionally, the intrinsic unsteadiness of the local flow poses a hazard for the release of the weapon. The aeroacoustic response is directly related to cavity geometry and freestream conditions [1] and under certain conditions, resonant modes are developed further aggravating the noise produced. The frequencies at which resonance occurs are called Rossiter modes, following early work on cavity flows [2]. The resonating frequencies are more generally predicted using the Rossiter-Heller equation [3], which accounts for compressibility effects,

$$f_n = \frac{U_\infty}{L} \cdot \frac{n - \xi}{M_\infty \left[1 + \frac{(\gamma-1)}{2} M_\infty^2\right]^{-1/2} + \frac{1}{K}} \tag{1}$$

Here $K$ is the ratio of disturbance velocity in the shear layer to the freestream velocity (generally taken as 0.57), and $\xi$ is an empirical constant employed to account for the phase lag between the passage of an eddy past the cavity trailing edge and the formation of an upstream travelling disturbance. The value of $\xi$ depends on the length-to-depth ratio ($L/D$) of the cavity and is evaluated as $\xi = 0.062(L/D)$ [2]. The ratio of specific heats, $\gamma$, is assumed to be equal to 1.4 for air.

Flow over a cavity has been a fundamental research topic and the influence of geometric parameters such as length-to-depth and width-to-depth ratios has been consistently explored [4]. Nevertheless, the aero-acoustic response of a weapons bay can strongly differ from the standard rectangular cavity. Typical weapons bay aerodynamic and acoustic response is strongly influenced by external factors, such as local design solutions, which alter the reference rectangular shape [5–12]. Dedicated studies have shown the strong influence of bay doors on the cavity. Typically, the doors increase the overall acoustic signature and tonal response [8, 13–16]. Another important factor is that in combat, military aircraft may operate the weapon bays at flight attitudes that typical experiments of "isolated" cavities do not account for. This is usually represented by non-zero angles of attack and sideslip, the effects of which on cavities have rarely been studied [17].

The present work seeks to expand previous studies on angle of attack effects on weapon bays, exploring the influence of this flow parameter in a geometry incorporating doors. Numerical analyses, at Mach numbers of 0.85 and 1.20 were conducted on a rectangular cavity with leading and trailing edge serrations (typical of low-RCS airframes) and 90-degree open doors installed. Additionally, the forces and moments induced on the doors by the unsteady flow field were recorded, and their spectrum was compared with the doors' modal analysis to explore fluid/structure coupling. The procedure consisted of using a one-way-fluid–structure interaction approach, where first the unsteady loads on the geometry (with the latter modelled as rigid) were computed. Subsequently, the modal analysis of the doors was conducted and the resonant frequencies were extracted. Finally, the critical frequencies of the modal analysis were compared to the cavity resonant modes to evidence potential interactions.

## 2 Numerical Method—CFD

### 2.1 Cavity Geometry

The adopted cavity model was derived from the well-known M219 geometry, having a length-to-depth ratio of five and a width-to-depth ratio of one. The new geometry, shown in Fig. 1 introduced a double chevron step, of 5 mm depth, at the front and rear walls. The angle of the indentations was specified as 45 degrees, typical of the value present in military aircraft subjected to radar signature suppression/control design philosophies. The step height was chosen assuming the hypothesis that enough room would have been available to accommodate bay doors in their closed position [17, 18]. The cavity was complemented by a set of 2 doors, opened at 90 degrees. The doors were separated, from the side surface of the cavity, by a gap of 1 mm.

The reference axis system for the cavity ($X_c, Y_c, Z_c$) had the origin coincident with the cavity leading edge, with the x–z plane coincident with the bay symmetry plane (see Fig. 1). On the other hand, the door axis system, in which accelerations were measured, was located at the door centre of gravity, as shown in Fig. 1. A single rake, consisting of 19 pressure probes, was placed on the cavity floor to monitor pressure signals. The probe positions ranged from $x/L$ =0.05 to $x/L = 0.95$ and were evenly spaced. For this study, it was decided to install the cavity on a support (see Fig. 2). Such an installation was considered a better representation to explore the angle of attack effects on a weapons bay-like geometry.

### 2.2 Numerical Simulation

The simulations in this study were performed using the SST-SAS turbulence model [19] within the ANSYS Fluent 2021R2 CFD code. The capability of this code and the turbulence model to properly address cavity flow has been previously demonstrated by Egorov, et al. [20].

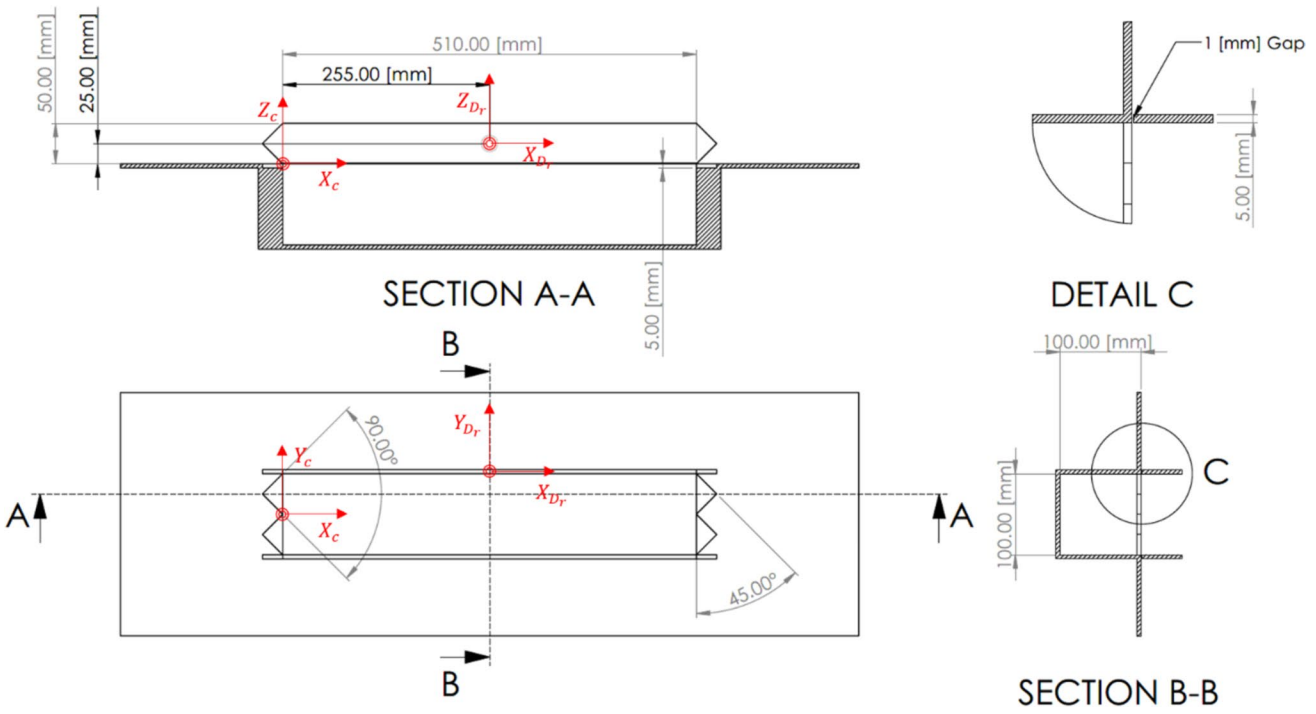


**Fig. 1** Cavity geometry and axes definition

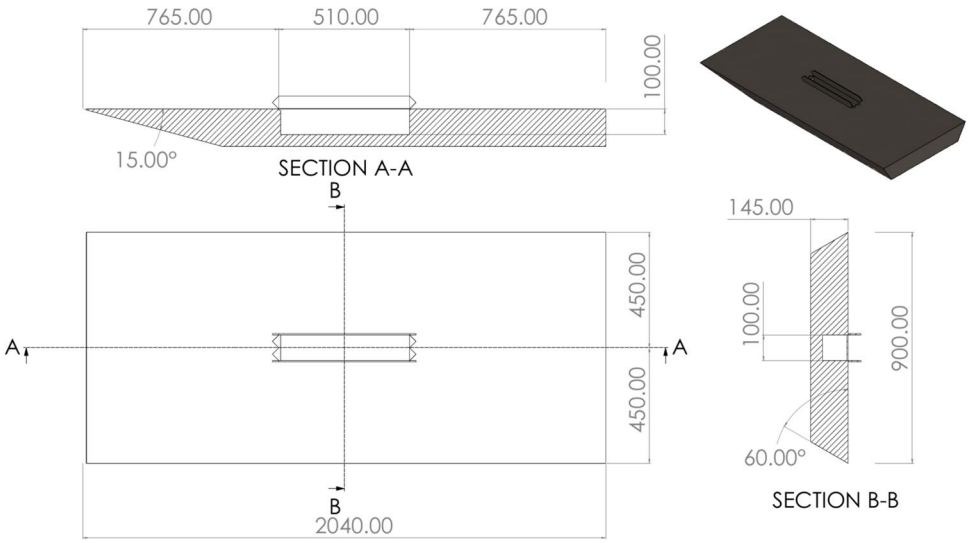


**Fig. 2** Cavity support geometry. Dimensions are in millimetres

The code uses the Favre-averaged version of the Reynolds-Averaged Navier Stokes Equations (RANS). Continuity, momentum and energy equations can be written as:

$$\frac{\partial \overline{\rho}}{\partial t} + \frac{\partial}{\partial x_j}\left(\overline{\rho}\widehat{u}_j\right) = 0 \tag{2}$$

$$\frac{\partial\left(\overline{\rho}\widehat{u}_i\right)}{\partial t} + \frac{\partial}{\partial x_j}\left(\overline{\rho}\widehat{u}_i\widehat{u}_j\right) = -\frac{\partial \overline{p}}{\partial x_j} + \frac{\partial \overline{\sigma}_{ij}}{\partial x_j} + \frac{\partial \tau_{ij}}{\partial x_j} \tag{3}$$

$$\begin{aligned}\frac{\partial\left(\overline{\rho}\widehat{e}\right)}{\partial t} + \frac{\partial}{\partial x_j}\left(\overline{\rho}\widehat{u}_j\widehat{h}\right) = &\frac{\partial}{\partial x_j}\left(\overline{\sigma}_{ij}\widehat{u}_i + \overline{\sigma_{ij}u_i''}\right) \\ &- \frac{\partial}{\partial_{xj}}\left(\overline{q}_j + C_p\overline{\rho u_j'' T''} - \widehat{u}_i\tau_{ij} + \frac{1}{2}\overline{\rho u_i'' u_i'' u_j''}\right)\end{aligned} \tag{4}$$

Here $h = e + p/\rho$ is the specific total enthalpy, $q$ is the heat flux, $C_p$ the specific heat capacity at constant pressure. The viscous stress and the Reynolds stress tensors are defined as:

$$\overline{\sigma}_{ij} \cong 2\widehat{\mu}\left(\widehat{S}_{ij} - \frac{1}{3}\frac{\partial \widehat{u}_k}{\partial x_k}\delta_{ij}\right) \tag{5}$$

$$\tau_{ij} = -\overline{\rho u_i'' u_j''} \tag{6}$$

In all the above equations the overbar represents the time-averaged mean, whilst the hat represents the density-weighted average, defined as:

$$\widehat{\phi} = \frac{\overline{\rho\phi}}{\overline{\rho}} \tag{7}$$

The terms $\tau_{ij}$, $C_p\overline{\rho u_j'' T''}$, $\overline{\sigma_{ij} u_i''}$, $\frac{1}{2}\overline{\rho u_i'' u_i'' u_j''}$ of Eqs. (3), (4), and (6) are addressed using the turbulence model. The two additional equations (required to close the model) are the ones of the $k-\omega$ *SST* model, proposed by Menter for which a detailed description (including the constant values) can be found in [21].

$$\frac{\partial \rho k}{\partial t} + \frac{\partial}{\partial x_i}\left(\rho u_i k\right) = G_k - \rho C_\mu k\omega + \frac{\partial}{\partial x_j}\left[\left(\mu + \frac{\mu_t}{\sigma_k}\right)\frac{\partial k}{\partial x_j}\right] \tag{8}$$

$$\begin{aligned}\frac{\partial \rho\omega}{\partial t} + \frac{\partial}{\partial x_i}\left(\rho u_i \omega\right) &= \frac{\alpha\omega}{k}G_k - \rho\beta\omega^2 + Q_{SAS} \\ &+ \frac{\partial}{\partial x_j}\left[\left(\mu + \frac{\mu_t}{\sigma_\omega}\right)\frac{\partial \omega}{\partial x_j}\right] + \left(1 - F_2\right)\frac{2\rho}{\sigma_{\omega,2}}\frac{1}{\omega}\frac{\partial k}{\partial x_j}\frac{\partial \omega}{\partial x_j}\end{aligned} \tag{9}$$

The governing equations of the SST-SAS model differ from those of the $k-\omega$ *SST* model by the additional source term ($Q_{SAS}$) in the right side of Eq. (9). This is given as,

$$Q_{SAS} = max\left[\rho\zeta_2\kappa S^2\left(\frac{L}{L_{vK}}\right)^2 - C\frac{2\rho k}{\sigma_\Phi}\cdot max\left(\frac{1}{\omega^2}\frac{\partial\omega}{\partial x_j}\frac{\partial\omega}{\partial x_j}, \frac{1}{k^2}\frac{\partial k}{\partial x_j}\frac{\partial k}{\partial x_j}\right), 0\right] \tag{10}$$

The constants are set as $\zeta_2 = 3.51$, $\sigma_\Phi = 2/3$, $C = 2$, $\kappa = 0.41$. In the above equation, $L$ is the length scale and $L_{vK}$ is the von-Karman length scale, defined as:

$$L = \frac{\sqrt{k}}{0.09^{0.25}\omega} \tag{11}$$

$$L_{vK} = \frac{\kappa S}{|U''|} \tag{12}$$

Here $S = \sqrt{2S_{ij}S_{ij}}$, with $S_{ij}$ being the strain rate tensor. The second derivative $|U''|$ is generalised to three-dimensions using the magnitude of the velocity Laplacian:

$$|U''| = \sqrt{\frac{\partial^2 U_i}{\partial x_k^2}\frac{\partial^2 U_i}{\partial x_j^2}} \tag{13}$$

The model also provides a direct control of the high-wave number damping. This is realised by inserting a lower constraint to the von-Karman length scale:

$$L_{vK} = \max\left[\frac{\kappa S}{|U''|}, 0.26\cdot\Delta\right] \tag{14}$$

As shown above, the limiter is proportional to the mesh cell size $\left(\Delta = (ControlVolume)^{\frac{1}{3}}\right)$. The purpose of this limiter is to control the damping of the finest resolved turbulent fluctuations [19].

The air was treated as an ideal compressible gas using Sutherland's law for viscosity modelling. Due to the compressible nature of the problem a pressure-based coupled solver was used. The coupled algorithm solves the momentum and pressure-based continuity equations together. The full implicit coupling is achieved through an implicit discretization of pressure gradient terms in the momentum equations, and an implicit discretization of the face mass fluxes. To interpolate cell-centered velocities to the faces, the code uses a modified version of the Rhie-Chow method [22, 23]. Regarding the discretization procedure, in the energy, $k$ and $\omega$ equations, convective terms were discretised with a second-order upwind scheme [24] whilst diffusion terms used a second-order central difference scheme [25]. The pressure equation used a second-order central difference scheme whilst, momentum adopted a bounded second-order scheme. Finally, the time marching scheme was an implicit bounded second-order using dual time formulation. Five inner sub-iterations were found to be adequate, which is consistent with the recommendation of Menter [26] and the approach of Chaplin and Birch [27].

The mesh was an unstructured polyhedral-type, with a prism layer wrapped around the viscous surfaces, for accurate boundary layer resolution, with a $y^+$ value of 1 or less. For accurate vortex structure modelling with scale resolving simulations, the detached shear layer was resolved using a spacing equal to 0.05 times its minimum thickness (i.e. at the cavity leading edge), as suggested by Menter [26]. The computational domain extended $6L$ to the right and left of support sides, $6L$ from the top and bottom limits of the support, and $8L$ upstream and $14L$ downstream from support leading and trailing edges respectively (see Fig. 3). All solid walls were specified as adiabatic surfaces where the no-slip condition was applied (Fig. 3A). The computational outer boundary was specified as a pressure far-field type (Fig. 3), using the modified Riemann invariants condition (see Table 1 for details).

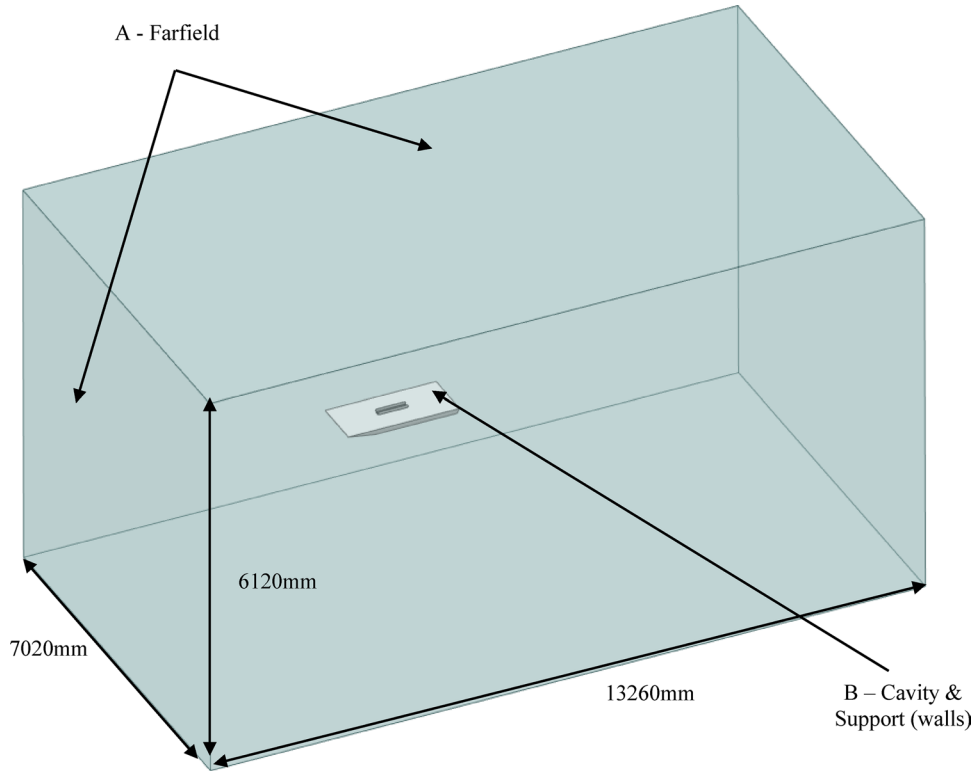


**Fig. 3** Computational domain

**Table 1** Test matrix and boundary conditions

| $M_\infty$ | $p_\infty[Pa]$ | $T_\infty[K]$ | $p_{0_\infty}[Pa]$ | $T_{0_\infty}[K]$ | $\alpha[deg]$ | $\beta[deg]$ | $k_\infty[m^2/s^2]$ | $\omega_\infty[1/s]$ |
|---|---|---|---|---|---|---|---|---|
| 0.85 | 63,177 | 266 | 101,325 | 300 | 0.0 | 0.0 | 2.9 | 378.1 |
| | | | | | 2.0 | | | |
| | | | | | 4.0 | | | |
| | | | | | 6.0 | | | |
| | | | | | 8.0 | | | |
| 1.20 | 41,784 | 233 | | | 0.0 | | 5.1 | 499.6 |
| | | | | | 2.0 | | | |
| | | | | | 4.0 | | | |
| | | | | | 6.0 | | | |
| | | | | | 8.0 | | | |

As advised by Menter [26], the time step was chosen to ensure a CFL number approximately equal to unity in the LES part of the domain. Unsteady simulations were initiated from a converged RANS solution to reduce the start-up time. To resolve accurately all the main features, the simulation was run for a total of 250 convective times ($t_c = L/U_\infty$), discarding the initial 100 $t_c$ s to clear the solution from the start-up transient. This allowed data sample lengths with a temporal duration greater than 30 cycles of the lowest frequency mode of interest (1st Rossiter-Heller Mode) following the values suggested by Menter [26].

## 2.3 Validation

To validate the computational settings and mesh convergence, data were used from wind tunnel studies of the M219 cavity [28]. and compared against a computational model of the same geometry. Three meshes were developed (coarse, medium, fine), and the results were compared to the experimental data (Fig. 4). There are small differences in the OASPL (see Eq. (21)) and SPL (see Eq. (22)). For OASPL these are of the order of 0.5 dB, between the medium and fine results, which is within the error band of the experimental data. Similarly, the SPL plot indicated that the medium and fine mesh could resolve the acoustic spectrum with sufficient precision, predicting

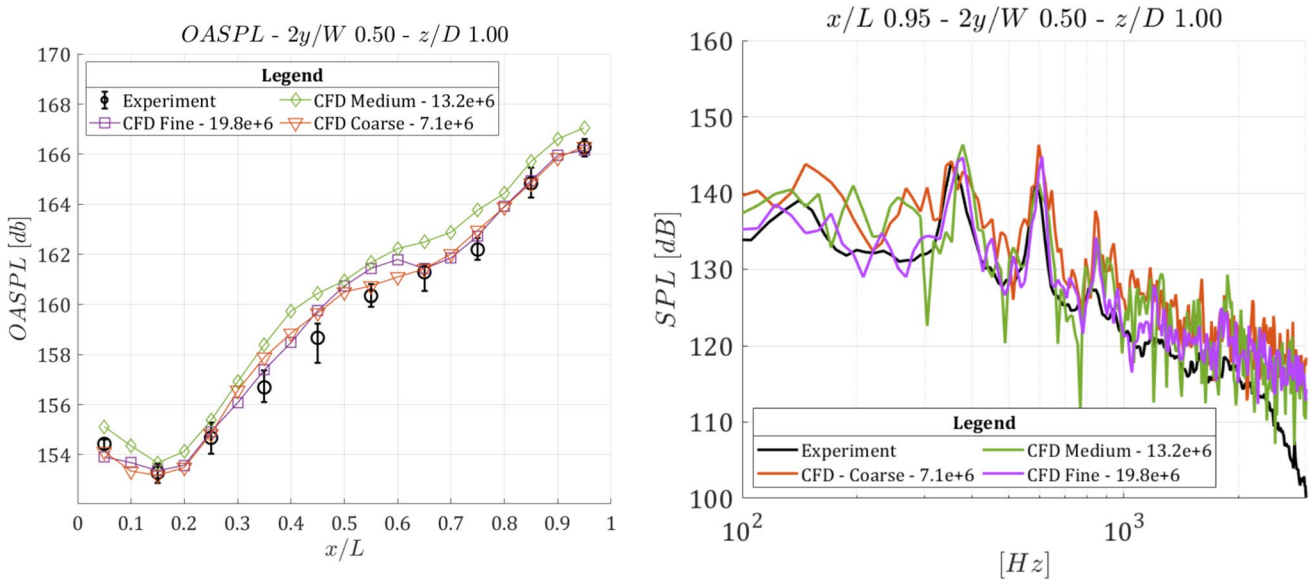


**Fig. 4** CFD grid convergence on OASPL (left)/SPL (right), and comparison with experimental data [28]. All data refers to the M219 geometry

the main resonant tone frequencies with an accuracy of ± 5 Hz and ±5 dB in comparison with experimental data. The level of agreement between the fine grid and the experimental data was considered adequate for this study, hence the fine mesh was used. This consisted of 19.8 million elements, of which 12.4 million were located inside the cavity.

To determine the resolution of turbulent scales for the LES part, the LESIQ (LES-Index of resolution Quality) approach was used [29]. This quantity was defined as the resolved portion of the turbulence kinetic energy:

$$\text{LESIQ} = \frac{k_r}{k_r + k_m} \tag{15}$$

Here the resolved kinetic energy ($k_r$) was directly computed from the mean square velocity fluctuations:

$$k_r = 0.5\left(\overline{u'u'} + \overline{v'v'} + \overline{w'w'}\right) \tag{16}$$

On the other hand, the time-averaged modelled sub-grid-scale kinetic energy was evaluated on the sub-grid-scale eddy viscosity $\mu_t$, density, and strain rate magnitude $S$:

$$k_m = \overline{\frac{1}{0.3}\frac{\mu_t}{\rho}S} \tag{17}$$

Figure 5 shows a slice (in the plane of symmetry) for the reference cavity using the fine mesh.

The shear layer and the great part of the cavity achieved a quality index of 0.75 or above, and, according to previous studies adopting the same turbulence model [20, 30], these values were considered satisfactory for the case.

The computational domains for all the other geometries (that included doors and leading/trailing edge indentations) were constructed following the same approach. The presence of the additional geometry features changed the overall mesh count and for the final geometry (incorporating the doors, the transverse edge indentations, and the door gaps) the overall total was 22.4 million elements of which 14.2 million were located inside the cavity.

## 2.4 Test Matrix

The cavity was tested at two representative Mach numbers within the transonic regime (0.85 and 1.20). The angle of attack was considered positive when the z-component of velocity in the cavity axis reference system (see Fig. 1) is negative. The sideslip angle was fixed at zero. The following table summarises the test matrix with the boundary conditions:

Regarding $k_\infty$, this was estimated as:

$$k_\infty = \frac{3}{2}\left(U_\infty I\right)^2 \tag{18}$$

Here $I$ is the free stream turbulence intensity, posed equal to 1%, typical of free-stream atmospheric flows. On the other hand, $\omega_\infty$ was computed as:

$$\omega_\infty = \frac{k_\infty^{0.5}}{0.09l} \tag{19}$$

Here $l$ is the turbulence length scale, which for these cases was set to half the cavity depth.

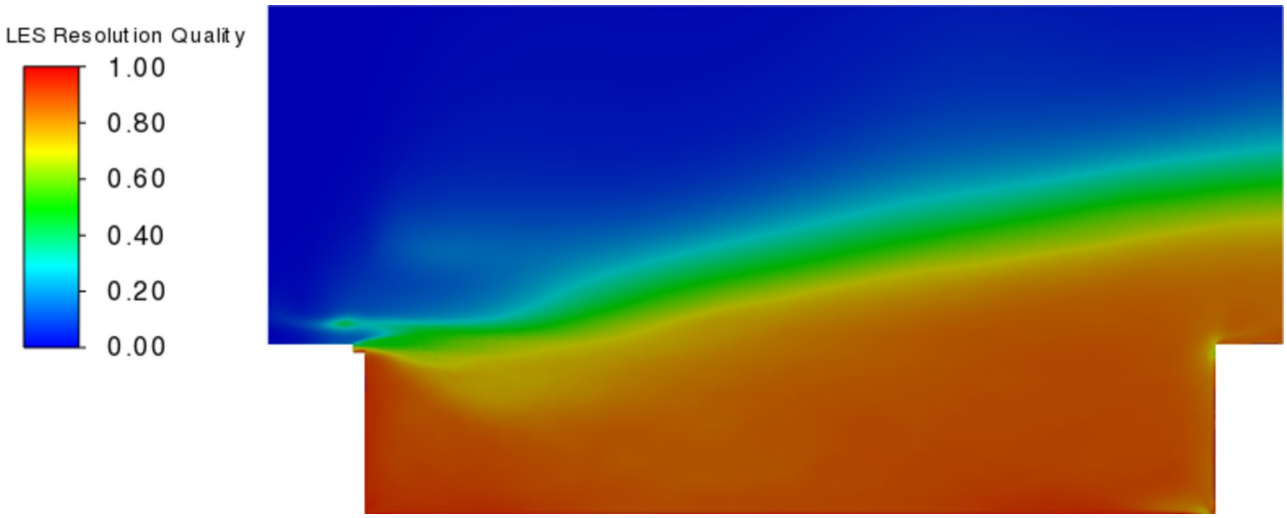


**Fig. 5** LESIQ contours for the fine mesh case ($M = 0.85$). Slice in the ZX symmetry plane. Flow from left to right

## 3 Numerical Method—Modal Analysis

The structural modal analysis was conducted only for the door geometry, as it was considered the most affected element in this configuration, and the loads are more affected by the flow.

### 3.1 Geometry

The door geometry used for the structural analysis was the same as for the CFD case, but it was complemented by the introduction of five rectangular bodies to represent the hinges, which in the simulation had the function of anchor points for the body (see Fig. 6). These cube-shaped additional parts, having 5 mm sides, and equally spaced across the door length were generated by comparing various weapons bay doors of existing combat aircraft. The idea was not to re-create an exact hinge model but to introduce similar constraints in the geometry deformation.

The mass and inertia properties of the door are listed in Table 2.

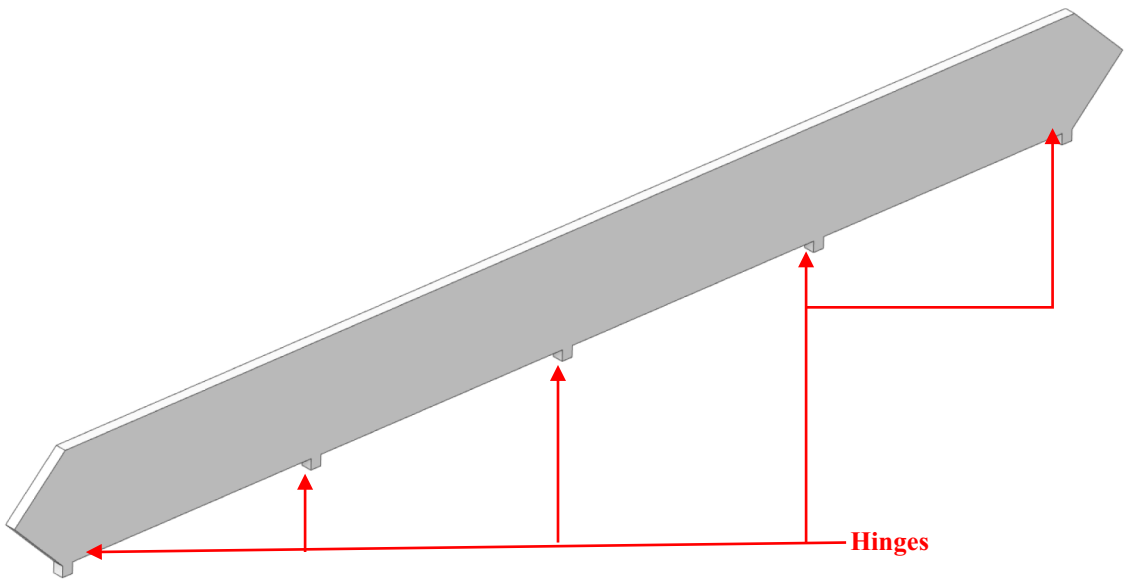


**Fig. 6** Door model used in the structural modal analysis

**Table 2** Door mass and inertia properties

| Property | Value | Units |
|---|---|---|
| $m$ | 0.3736 | [kg] |
| $I_{xx}$ | 7.77e− 5 | [kgm$^2$] |
| $I_{yy}$ | 9.02e− 3 | [kgm$^2$] |
| $I_{zz}$ | 8.94e− 3 | [kgm$^2$] |

### 3.2 Numerical Simulation

Modal analysis was conducted using ANSYS Mechanical ADPL 2021R2 code. The door body was discretised using hexahedral elements, imposing a minimum mesh size of 1 mm. This resulted in a total of 99,000 elements, with the door thickness discretised with at least six nodes. A rigid contact boundary condition was placed at the bottom face of the hinges. The mode extraction method used the undamped approach. The material selected for this study was 2024 aluminium alloy. The number of modes extracted was iteratively increased until the cumulative effective mass fraction reached one for all six motion components $(u_x, u_y, u_z, \theta_x, \theta_y, \theta_z)$ [31]. This corresponded to the extraction of 20 modes.

## 4 Data Analysis Procedure

### 4.1 Flow Analysis

The mean flow analysis consisted of the study of the mean pressure coefficient $\overline{C_p}$ and the overall sound pressure level (OASPL):

$$\overline{C_p} = \left\langle \frac{2}{\gamma_{air} \cdot M_\infty} \cdot \left[ \frac{p}{p_\infty} - 1 \right] \right\rangle \tag{20}$$

$$\text{OASPL} = 20 log_{10}\left( \frac{\sigma_p}{p_{\text{ref}}} \right) \tag{21}$$

Here $p_{\text{ref}}$ is the minimum audible pressure, defined as the threshold of human hearing, and equal to $2 \times 10^{-5}$ Pa. The non-stationary flow analysis was based on the study of the sound pressure level (SPL) of the fluctuating part of the pressure signals, which was defined as:

$$\text{SPL}(f) = 10 log_{10}\left( \frac{\text{PSD}(f)}{p_{\text{ref}}^2} \right) \tag{22}$$

The power spectral density (PSD) was obtained using the Welch method [32], with the division of the original signal in smaller blocks of 50% overlap, and with the number of samples equal to the closest power of two of the ratio of $f_s/f_r$.[1]

### 4.2 Bay Door Load Analysis

The door mean and unsteady loads generated by flow unsteadiness were reported in terms of acceleration and angular acceleration in the door axis reference system (see Fig. 1). The relative spectra $a(f)$ and $\dot{\omega}(f)$ were calculated as follows:

$$a(f) = \frac{2|\hat{a}|}{N} \tag{23}$$

$$\dot{\omega}(f) = \frac{2\left|\hat{\dot{\omega}}\right|}{N} \tag{24}$$

Here $\hat{a}$ and $\hat{\dot{\omega}}$ are the one-sided FFT of the acceleration and angular acceleration signals, whilst $N$ is the number of samples of the time series. This approach allowed the spectra to be expressed in units of $\frac{\text{m}}{\text{s}^2}/\text{Hz}^{1/2}$ and $\frac{\text{rad}}{\text{s}^2}/\text{Hz}^{1/2}$.

### 4.3 Coherence Analysis

Given two signals $x(t)$ and $y(t)$, with their relative Fourier transforms $X(f)$ and $Y(f)$, the coherence $\text{CSP}_{\text{xy}}(f)$ can be defined as:

$$\text{CSP}_{\text{xy}}(f) = \frac{\left|X(f) \cdot Y(f)'\right|^2}{|X(f)|^2 |Y(f)|^2} \tag{25}$$

Here $Y'(f)$ is the Hermitian transpose of $Y(f)$. The coherence varies between 0 to 1 and expresses the correlation between $x(t)$ and $y(t)$ at each frequency. For this study, this quantity was used to correlate the linear and angular accelerations of the pressure signals imposed by the flow on the doors to isolate the frequency bands responsible for the majority of the energy transfer. As in the case of $SPL$, the spectral densities were obtained using the Welch method [32], with the division of the original signal in smaller blocks of 50% overlap, and with the number of samples equal to the closest power of two of the ratio of $f_s/f_r$.[2]

[1] The frequency resolution was posed equal to 20 Hz.

[2] The frequency resolution was posed equal to 20 Hz.

# 5 Results

## 5.1 Aero-Acoustic Analysis

### 5.1.1 Mean Flow Analysis

The evolution of $\overline{C}_p$ in the cavity's longitudinal dimension, at zero angle of attack, had a trend in line with the open-type cavity [4] at both Mach numbers. For Mach 0.85, the curve had a negative gradient in the front part of the bay up to $x/L = 0.4$, with values ranging from $-0.026$ to $-0.064$. Past this point, the gradient's sign was reversed with $\overline{C}_p$ values increasing up to a value of 0.044 at the rear of the cavity (Fig. 7).

On the other hand, at Mach 1.20, the curve changed and the minima at $x/L = 0.4$ disappeared. The mean pressure coefficient assumed a constant value of -0.03 up to $x/L = 0.35$, rising to 0.077 at the rear of the cavity. When the angle of attack was introduced it was observed that, whilst the qualitative trend of $\overline{C}_p$ remained unchanged, each increment of incidence progressively translated the curve towards higher values.

The analysis of the cumulative difference between each angle of attack increment step was used to quantify this trend. Cumulative difference ($d_k$), expressed as a series, was defined as follows:

$$d_k = \sum_{i=2}^{k} \left(y_i - y_{i-1}\right) \qquad d_1 \equiv 0 \tag{26}$$

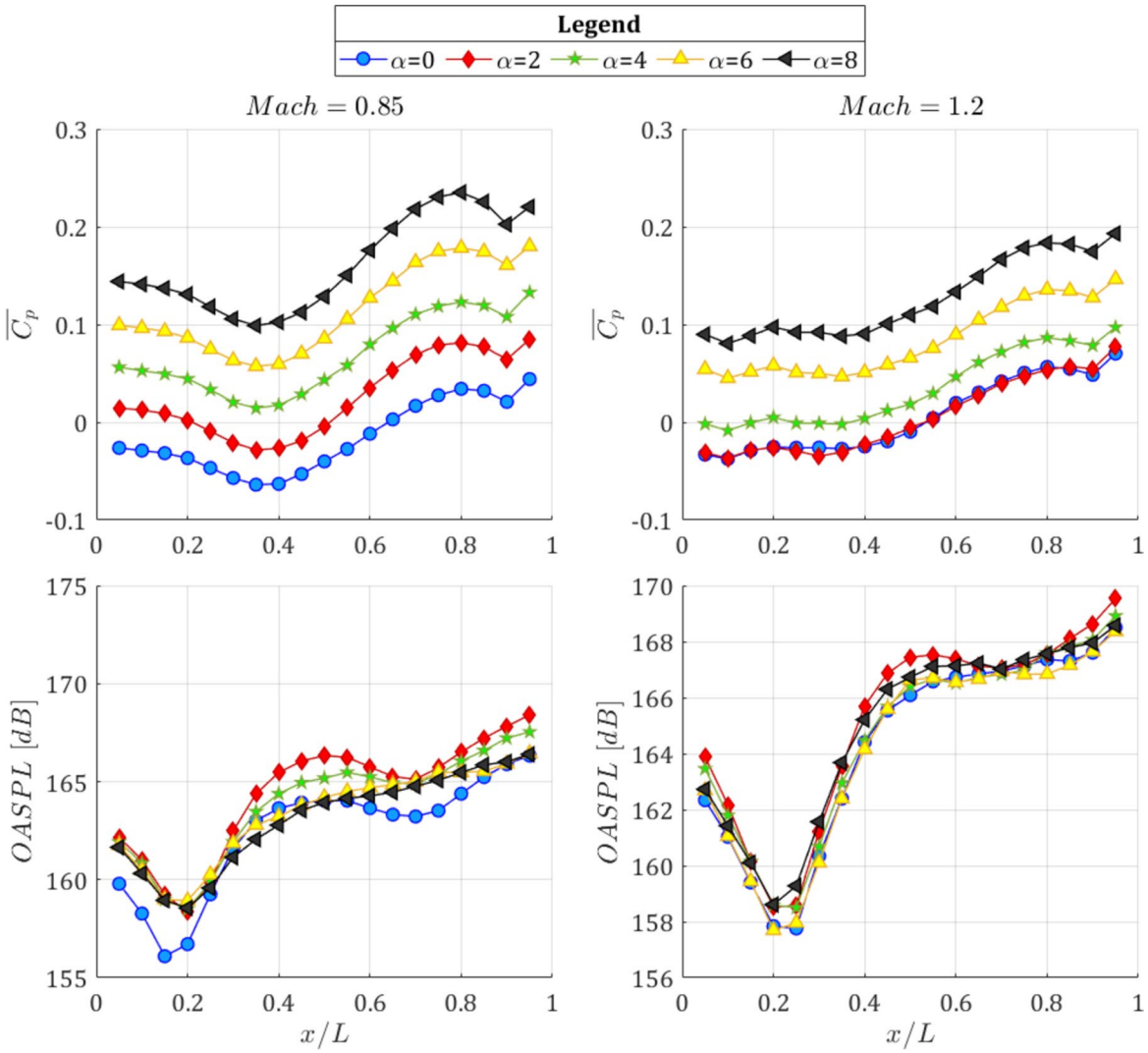


**Fig. 7** Mean pressure coefficient and OASPL comparison. Left column, Mach = 0.85. Right column, Mach = 1.20

$$y_i = \frac{1}{L}\int_{x=0}^{x=L} \overline{C}_p(x)_{\alpha=i} dx \tag{27}$$

Here the quantity $y_i$ is the rake-averaged value for the mean pressure coefficient at the $i^{th}$ angle of attack. This series was used to calculate how much the $\overline{C}_p$ value varied, compared to the zero incidence case, as the angle of attack was increased.

As shown in Fig. 8 the trend was very similar for both Mach numbers, leading to the conclusion that the variations in the mean pressure coefficient inside the cavity were directly correlated to the appearance of a vertical (i.e. directed inwards) component of the freestream velocity vector. The only exception was $\alpha = 2$ at Mach = 1.20. In this case, the variation compared to $\alpha = 0$ deg was practically null.

The influence of the angle of attack on acoustic effects was also evident (Fig. 7), but the trend, in this case, was different between the subsonic and the supersonic regime. At Mach 0.85, varying incidence from 0 to 2 deg caused an increase of 2 dB at stations between $x/L = 0.05$ to 0.2, and between $x/L = 0.4$ to 0.95. By contrast OASPL did not change between $x/L = 0.25$ and 0.35. Placing the cavity at higher angles of attack did not change the OASPL values in the front part of the cavity (up to $x/L = 0.3$). On the other hand, the rear and central part of the cavity experienced a progressive reduction of acoustic noise upon progressing towards higher angles of attack, up to the point where similar levels to the zero angle of attack case were attained. At Mach 1.20, the overall effect of the angle of attack was an increase of 1 dB to 2 dB when passing from $\alpha = 0$ deg to $\alpha = 2$ deg. At $\alpha = 4$ deg, on the other hand, the overall levels reduced again. From $\alpha = 4$ deg to $\alpha = 6$ deg no appreciable variation was observed, whilst finally moving from $\alpha = 6$ deg to $\alpha = 8$ deg another increase of OASP was recorded.

The trend observed could be partially explained by analysing the boundary layer thickness ($\delta$) at the cavity leading edge. As shown in Fig. 9, increasing the angle of attack, affected boundary layer height. At Mach 0.85, $\delta$ decreased from 9 mm to 8.6 mm when incidence passed from 2 to 4 deg, but remained almost unchanged after this point. This result was in line with the Falkner-Skan boundary layer solution over a wedge (to which the plate in front of the cavity, as incidence increased, could be compared). For the angles of attack explored in this study, the theory predicts a variation in boundary layer thickness between zero and eight degrees AoA of only 0.73%. Conversely, at Mach 1.20, boundary layer thickness experienced strong variations. Starting from $\delta = 13$ mm at zero angle of attack, the boundary layer thickness is reduced to 10 mm at $\alpha = 2$ deg, following again theory predictions. Subsequently, thickness increased to a new value of 16 mm at $\alpha = 4$ deg and 24 mm at $\alpha = 6$ deg. This was due to the detachment of the shock. The oblique shock theory, for a Mach number of 1.2, admits an attached shock solution only for a deflection angle of up to 3.9 degrees approximately. Passed this value, the shock is detached, hence explaining the increase of boundary layer thickness observed. Finally, at $\alpha = 8$ deg $\delta$ decreased again to 20 mm. This was due to the complete detachment of the shock from the leading edge of the cavity support. The downstream flow, along with the development of the boundary layer on the planar

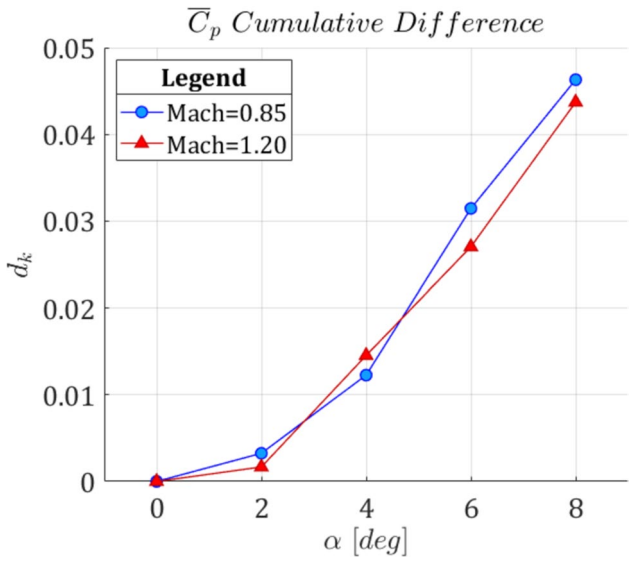


**Fig. 8** Influence of angle of attack on the cumulative difference trend for the mean pressure coefficient averaged over the whole rake

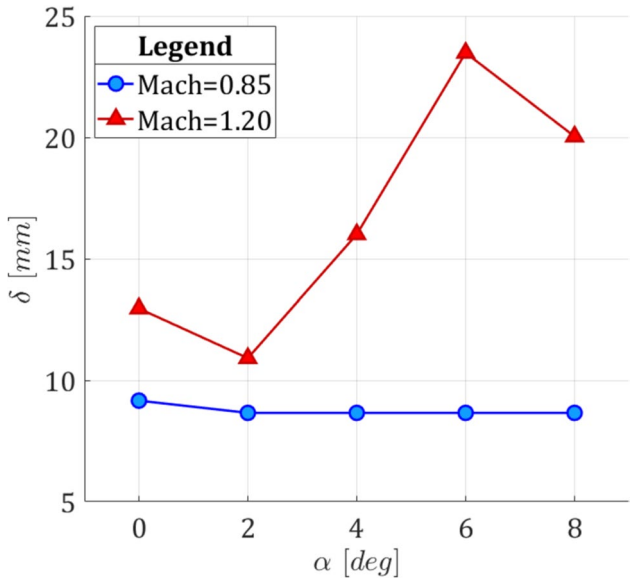


**Fig. 9** Influence of angle of attack on the boundary layer thickness at the cavity leading edge

surface, resumed the previous trend, and in accordance with the Falkner-Skan self-similarity solution, the thickness decreased again with increasing incidence.

Previous studies [33, 34] indicated that boundary layer thickness influences the acoustic response of a cavity. In general, high values of $\delta/D$ ratios induce a damping effect, reducing acoustic oscillations and the appearance of resonant modes, whilst the opposite is true for low values of $\delta/D$. Although the exact value of this ratio varies according to environmental conditions, it is common agreement that, keeping freestream conditions and cavity geometry unchanged, an increase of boundary layer thickness has the effect of reducing the radiated noise. Regarding the current study, a direct effect of boundary layer thickness was indeed observed. As shown in Table 3, at Mach 0.85, each increase in boundary layer thickness from one incidence to the next corresponded to a decrease of $\overline{\text{OASPL}}$ (this quantity represents the average OASPL across the longitudinal rake) and the OASPL value at $x/L = 0.95$ (the point in the rake experiencing the highest amplitude). The relationship was not only qualitative but also quantitative since greater variations in $\delta$ corresponded to larger changes in OASPL. On the other hand, at Mach 1.20, the situation was different. Although, from a qualitative point of view, it could still be stated that an increase/decrease of boundary layer thickness led to a decrease/increase in OASPL levels, the same proportionality observed at Mach 0.85, was no longer present. Furthermore, when local OASPL variations were observed, moving from 6 deg. to 8 deg. angle of attack, did not result in an increase in OASPL (at $x/L0.95$) but to a decrease, although the boundary layer thickness did decrease. The different behaviour indicated that, in the supersonic regime, additional factors influenced the acoustic response of the cavity in addition to boundary layer thickness variations.

The line integral convolution (LIC) technique [35] was used to gain further insight into mean flow topology. Figure 10 compares the flow pattern at Mach 0.85, between angles of attack of 2 and 4. It was observed that the interior of the cavity was dominated by a clockwise main vortex, which occupied up to 50% of the cavity volume. The centre of this main vortex did not change appreciably with an angle of attack. Such behaviour was the direct cause of the invariance of the $\overline{C}_p$ streamwise distribution with angle of attack. Nevertheless, minor changes were observed, explaining the change in acoustic power emitted at different incidences. Such changes correlated well with variations of $\delta$, as boundary layer thickness variations directly affect the vorticity injected in the shear layer and so the overall recirculation inside the cavity. In turn, whilst, the overall vortex shape was not changed, the magnitude did, and the mean pressure plots were translated progressively at each increment of incidence as shown in Fig. 7.

Flow topology at Mach 1.20 was essentially unaffected by angle of attack variations, and apart from the front shock, no changes were observed inside the cavity upon varying the angle of attack (see Fig. 11). The eddy structure inside the cavity was still composed of a major clockwise vortex, accompanied by two smaller eddies, located at the cavity front and rear walls. Angle of attack variations did not change the impact point of the shear layer at the rear of the and the changes in the position of the main recirculating eddy were barely noticeable. This result was a direct consequence of the invariance of the OASPL curve with angle of attack as reported in Fig. 7, as well as the lower influence, on acoustic emission, due to $\delta$ changes, respect to the transonic case.

The LIC technique was also coupled with the OASPL contours (Figs. 12 and 13). Slices along the cavity symmetry plane (Fig. 12-Left) indicated a marked increase in acoustic levels (orange/red contours) in the cavity centre and rear zones, upon increasing incidence to 2 deg. Further increase in angle of attack reversed the trend and the high-OASPL area began to shrink. This was accompanied by a reduction in the acoustic power emitted outside the cavity area (green-coloured contours). At supersonic Mach number (Fig. 12-Right) the effects of angle of attack were different. In this case, the high-OASPL contour did not vary appreciably. Instead, it was the front shock, generated by the cavity leading edge, which experienced dependence

**Table 3** Correlation between boundary layer thickness variations, averaged OASPL variations, and local OASPL variations (at $x/L = 0.95$) between consecutive incidence steps

| Variation in AoA [deg] | Mach = 0.85 | | | Mach = 1.20 | | |
|---|---|---|---|---|---|---|
| | $\Delta\delta$[mm] | $\Delta\overline{\text{OASPL}}$ [dB] | $\Delta\text{OASPL}_{x/L^{0.95}}$ [dB] | $\Delta\delta$[mm] | $\Delta\overline{\text{OASPL}}$ [dB] | $\Delta\text{OASPL}_{x/L^{0.95}}$ [dB] |
| 0 → 2 | − 0.50 | + 1.97 | + 2.08 | − 2.04 | + 0.85 | + 1.04 |
| 2 → 4 | + 0.04 | − 0.52 | − 0.87 | + 5.09 | − 0.50 | − 0.63 |
| 4 → 6 | + 0.03 | − 0.48 | − 1.09 | + 7.48 | − 0.39 | − 0.58 |
| 6 → 8 | + 0.01 | − 0.27 | − 0.05 | − 3.45 | + 0.21 | − 0.22 |

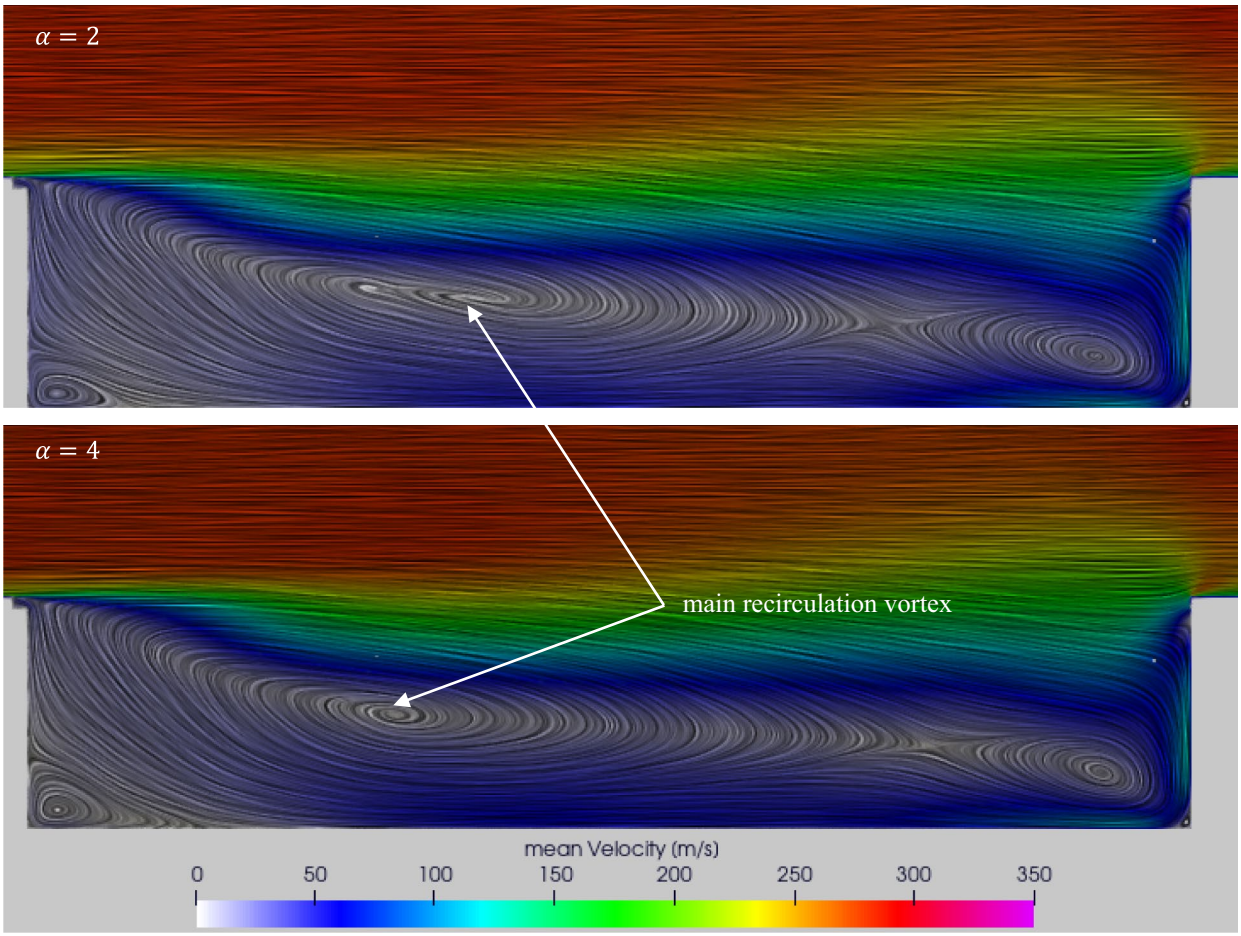


**Fig. 10** LIC of mean flow velocity, coloured by velocity magnitude. Slice at $2y/W = 0$. Comparison of topology between $\alpha = 2$ (upper) and $\alpha = 4$ (lower). Mach 0.85. Flow from left to right

on incidence. The reference pattern, at $\alpha = 0$, consisted of a small (in terms of extension into the flow) normal shock, followed by a large oblique one. Upon increasing incidence, whilst the shape and size of the oblique shock remained unchanged, the front normal shock began to extend further into the flow, reaching a maximum extension at $\alpha = 4$. Passed this point, the normal shock shrunk to a size smaller compared to the case at zero angle of attack.

Flow effects on the area surrounding the cavity were analysed using a slice of the flow domain in correspondence with the cavity entry plane (Fig. 13). At Mach 0.85, the major effect caused by the increasing angle of attack was represented by the extension of the area, outside the cavity perimeter, exposed to OASPL values higher than 150 dB (green and yellow coloured contours).

In the front part of the cavity, close to the door leading edge, the amount of flow spillage (moving from inside to the outside of the cavity, through the door gap), and consequent associated acoustic load, increased consistently with angle of attack. Conversely, on the rear part, OASPL increased from $\alpha = 0$ to $\alpha = 2$ but reversed the trend if incidence was further increased.

The flow features at Mach 1.20 were largely unaffected by angle of attack variations, except for the footprint of the normal shock at the cavity leading edge. This followed a pattern similar to the one observed in Fig. 12. The footprint (seen from above) did not present peculiar differences if incidence was varied between 0 to 2 and between 6 to 8 degrees. The opposite was observed for $\alpha = 4$. Here the footprint was different and a second bow shock appeared as shown in Fig. 13 (right column).

#### 5.1.2 Unsteady Flow Analysis

Spectral analysis conducted on the region of the cavity with the highest OASPL (probes at $x/L$=0.95) indicated that at Mach 0.85 three main tones, corresponding to Rossiter-Heller modes, were present as shown in

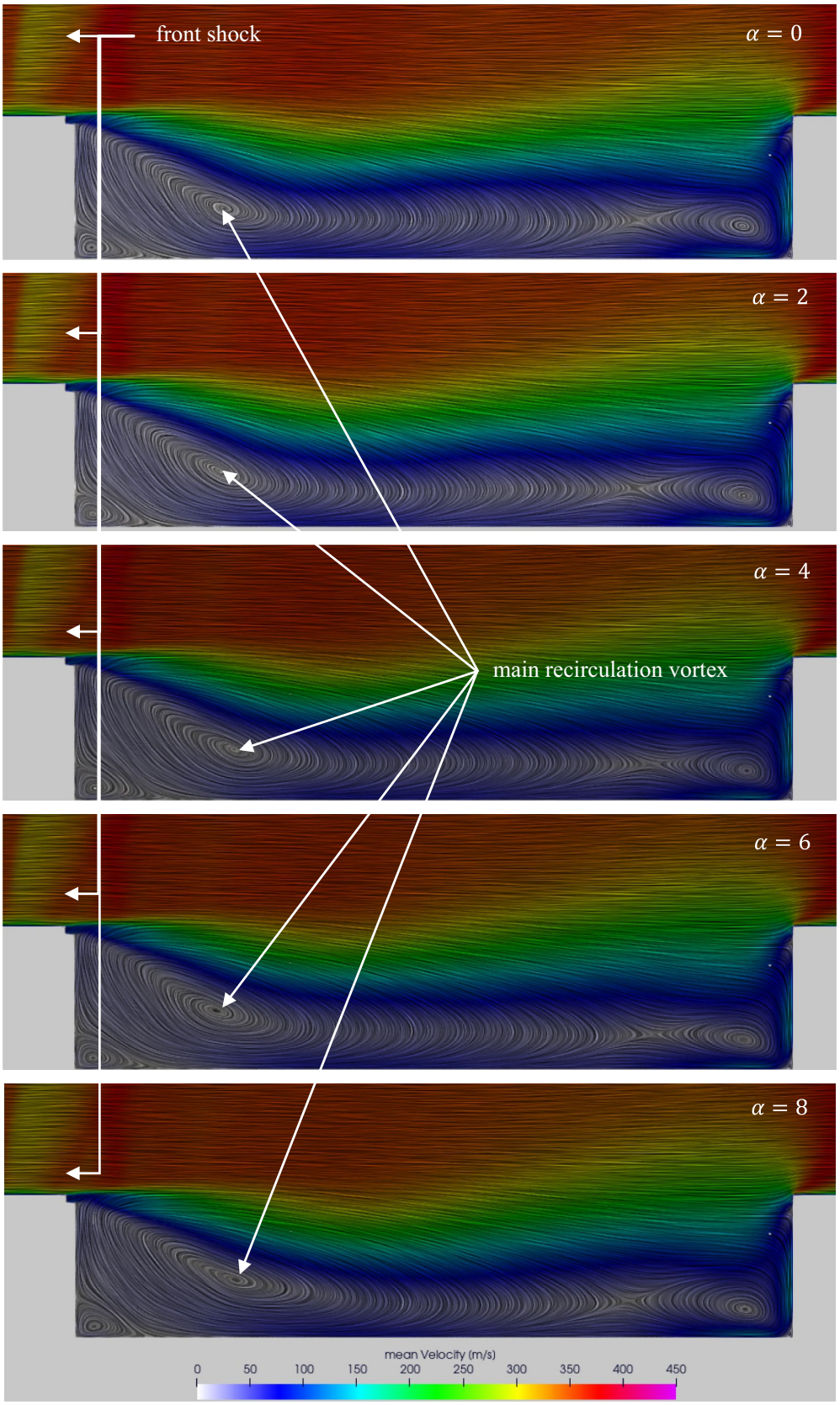


**Fig. 11** LIC of mean flow velocity, coloured by velocity magnitude. Slice at $2y/W$=0. Comparison of topology at different angles of attack. Mach 1.20. Flow from left to right

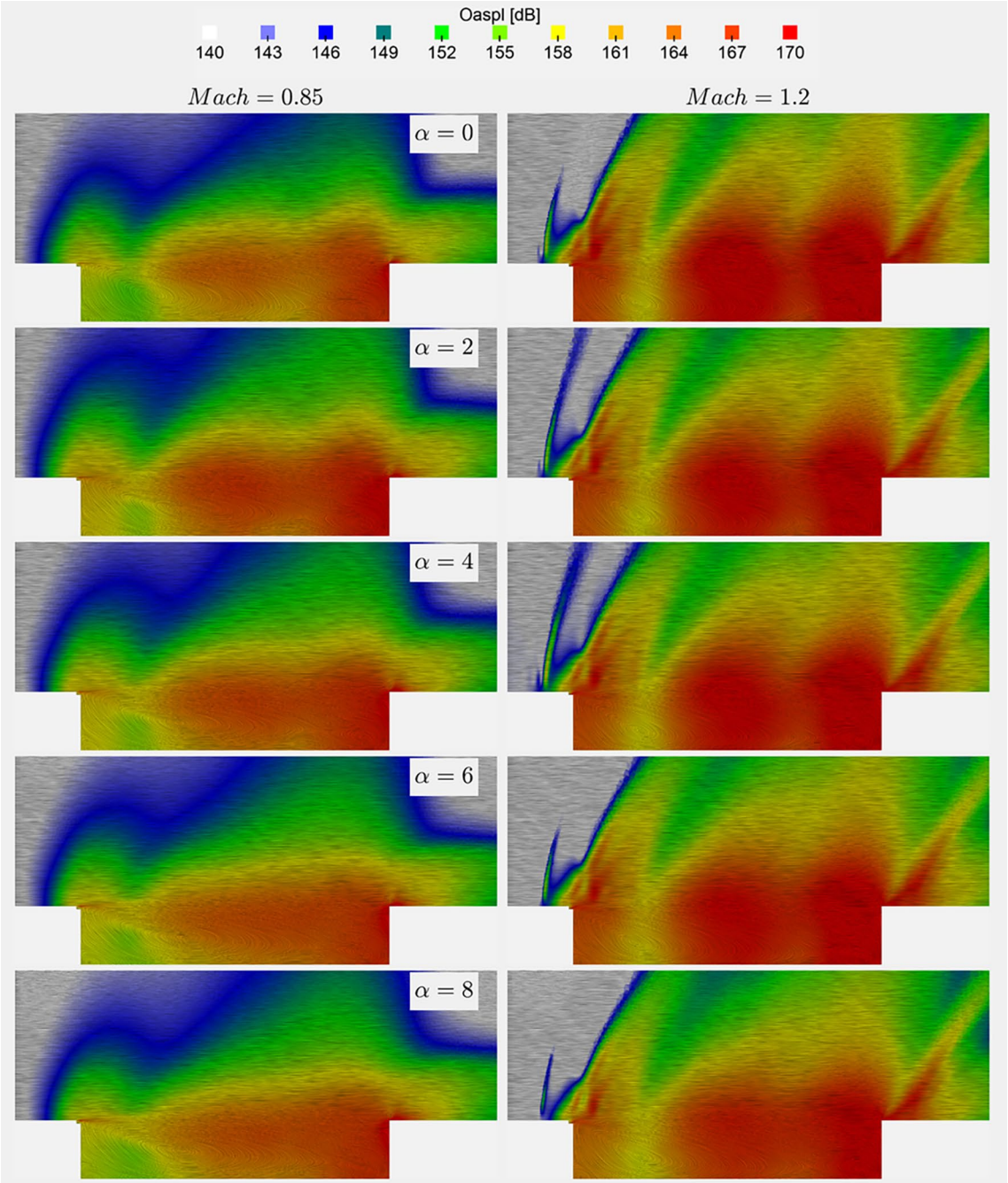


**Fig. 12** Comparison of mean flow velocity LIC coloured by OASPL (Mean-flow-velocity LIC coloured by OASPL: the mean velocity flow vector lines were integrated using Line-Integral-Convolution technique to visualise the flow pattern. This was then coloured by the corresponding OASPL value.). Slice at $=2y/W0$. Flow from left to right. Left column, angle of attack sweep at Mach 0.85. Right column, angle of attack sweep at Mach 1.20

Fig. 14. Whilst the theory (Eq. 1) predicted these values at 151 Hz, 364 Hz, and 577 Hz, computational data located the modes at 159 Hz, 378 Hz, and 549 Hz respectively. Such differences could be explained by the presence of chevrons and doors, whose effects on the rectangular cavity have already been studied and observed [8, 15, 36, 37]. Considering the RH tones for the standard M219 cavity, at Mach 0.85, these were: 141 Hz/139 dB ($R_1$), 351 Hz/144 dB ($R_2$), 597 Hz/141 dB ($R_3$). All these values were consistently different from the values obtained in the current cavity (incorporating doors and chevrons) at Mach 0.85 159 Hz/137 dB ($R_1$), 378 Hz/145 dB ($R_2$),

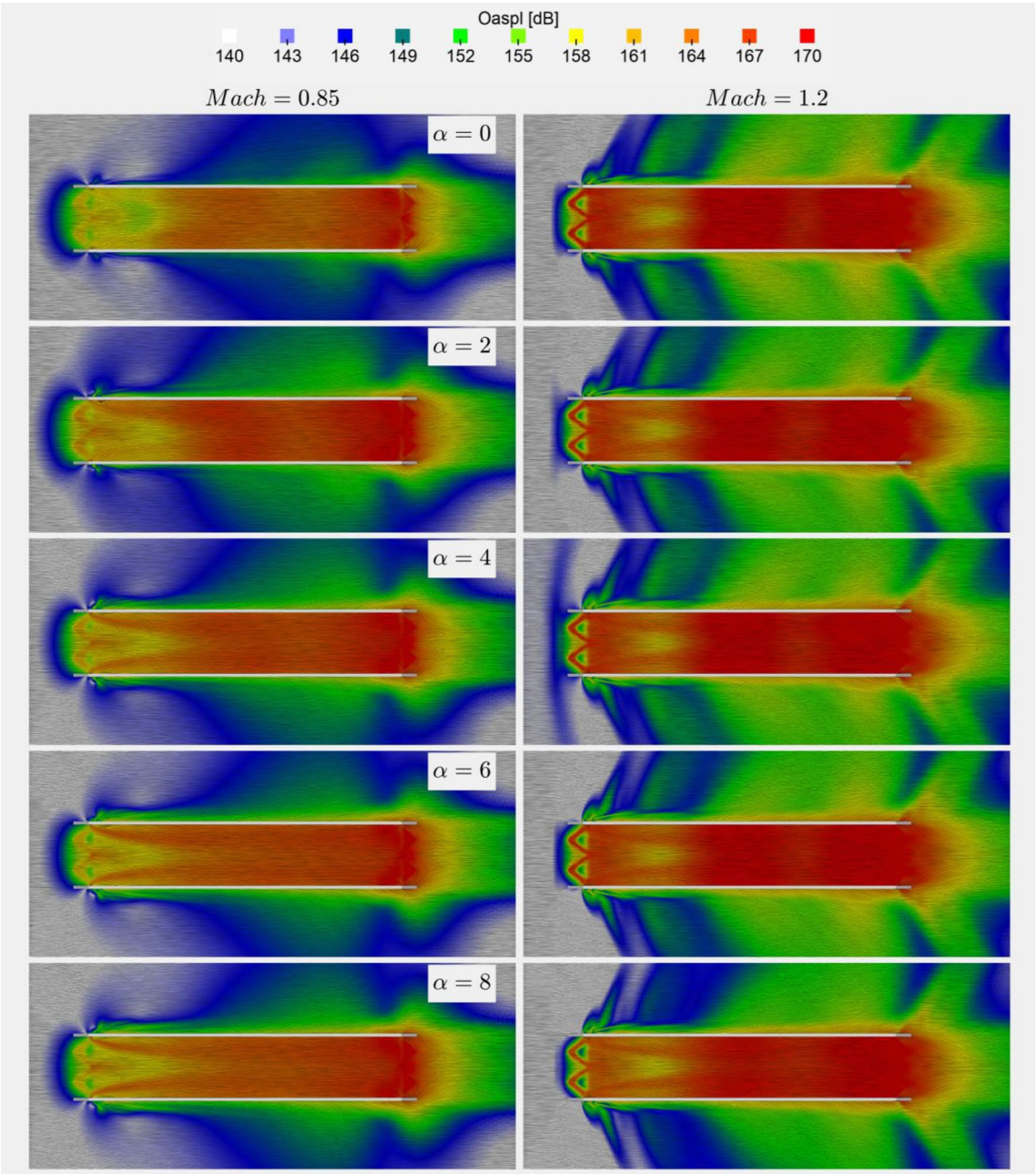


**Fig. 13** Comparison of mean flow velocity LIC coloured by OASPL. Slice at $z/D$=0. Flow from left to right. Left column, angle of attack sweep at Mach 0.85. Right column, angle of attack sweep at Mach 1.20

549 Hz/142 dB ($R_3$). The conclusion was that the main shift from RH theory predictions, at zero angle of attack, was due to geometry effects.

SPL levels indicated $R_2$ as being the dominant mode, with an amplitude of 145.2 dB, whilst $R_1$ and $R_3$ power was 136.7 dB and 142.1 dB respectively. Increasing incidence ($\alpha = 2$) slightly changed the peak locations in the frequency $R_2$, with an associated change in power which rose to 148.5 dB. $R_1$ and $R_3$ changed the frequency location and the associated power. $R_1$ moved to 183 Hz and raised its power to 138.7 dB, whilst $R_3$ moved to 574 Hz and decreased the power to 139.6 dB. At $\alpha = 4$, $R_2$ and $R_3$ decreased their power to 146.5 dB and 138.1 dB respectively. $R_3$ did also changed frequency, to 598 Hz. On the other hand, $R_1$, whilst not changing frequency, increased its associated power to 139.7 dB. Further increases in the angle of attack induced a decrease in power to $R_2$ and $R_3$ that achieved a minimum at $\alpha = 8$, with 142.3 dB and 136.1 dB respectively. Conversely, $R_1$, whilst decreasing in power as angle of attack was increased like $R_2$ and $R_3$, also shifted in frequency; 159 Hz

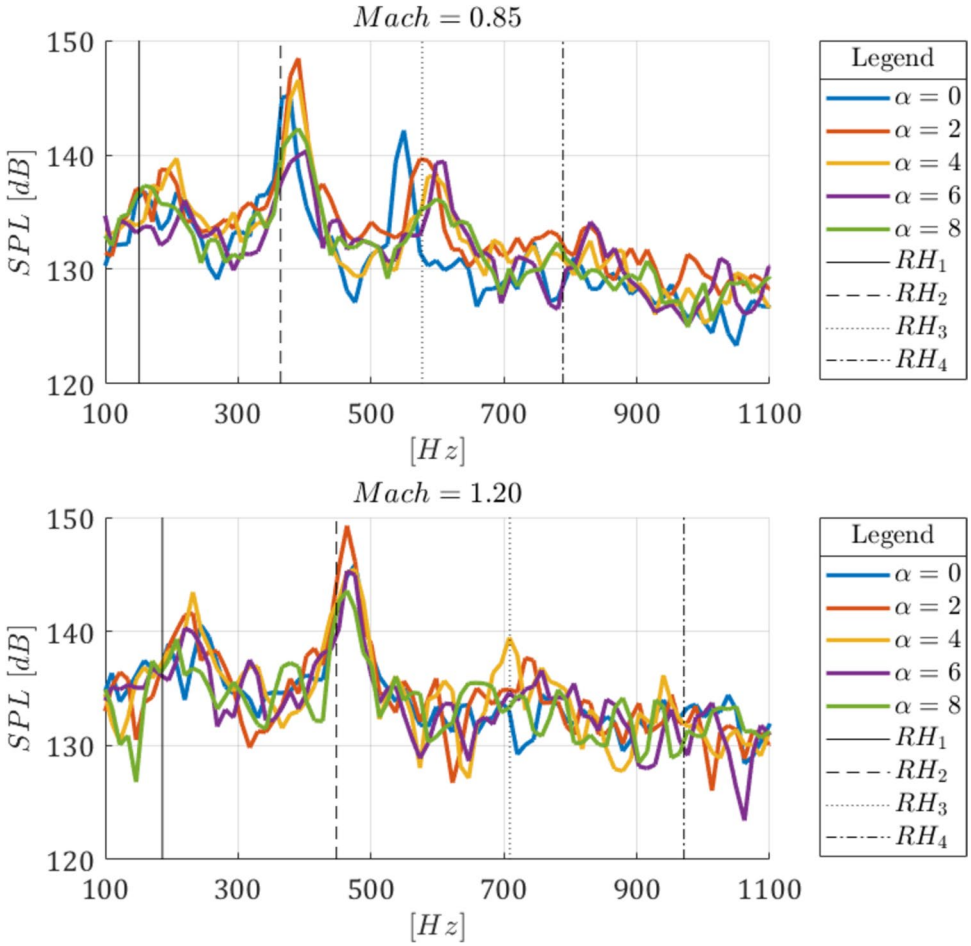


**Fig. 14** SPL comparison for probe located at $x/L = 0.95$, $2y/W = 0.00$, $z/D = 1.00$. Upper figure, Mach 0.85. Lower figure, Mach 1.20. Black-coloured vertical lines represent predicted Rossiter-Heller modes

at $\alpha = 6$ and 220 Hz at $\alpha = 8$. The maximum (in terms of Rossiter-Heller mode power) was observed for $\alpha = 2$, and it was always associated with $R_2$.

At Mach 1.20, the spectra of the pressure signal inside the cavity were characterised by two resonant tones, corresponding to the 1st and 2nd Rossiter-Heller modes. These were respectively $R_1$(140.5 dB, 244 Hz), and $R_2$ (145.8 dB, 476 Hz). Only $R_2$ was in line with the theoretically predicted value, whilst $R_1$ consistently deviated from it. The deviation of $R_1$ from the theory was attributed to the presence of chevrons at the leading edge of the cavity and the associated saw-toothed doors. As shown in the mean-flow analysis these generated a complex shock structure that could have influenced a large-scale mode such as $R_1$, with a wavelength typically greater than the cavity length. On the other hand, $R_2$ with a wavelength slightly shorter than the cavity length and higher power, would have less likely been influenced by the shock pattern and indeed had a frequency in line with the theory-predicted value. Increasing the incidence to $\alpha = 2$ increased the power of $R_1$ and $R_2$ to 141.6 dB and 149.3 dB respectively. Also, a new resonant mode, associated with the 3rd RH tone appeared, at 732 Hz with a SPL of 137.7 dB. At $\alpha = 4$ and $\alpha = 6$ the spectrum was similar to the zero incidence case. The sole difference was that the 3rd mode, $R_3$ remained. Finally, further increasing the angle of attack up to 8 deg, whilst not appreciably changing $R_1$ considerably, consistently reduced the power of $R_2$ (143.6 dB at $\alpha = 8$). Also, at these angles of attack $R_3$ was barely distinguishable from the background noise.

Previous studies already showed that the formation of RH modes is a complex non-linear phenomenon [38–40]. Hence, whilst boundary layer thickness plays a major role in cavity acoustic response, angle of attack variations influence other mechanisms of resonant mode generation as well. As already shown in previous studies [17], the carrier frequency and modulating frequencies, derived using Delprat's decomposition [39], can be correlated directly with the sine of the angle of attack. Considering that changes in such frequencies affect the resulting resonant modes, it was likely that for this case a similar effect was occurring.

According to Delprat's decomposition the carrier frequency $f_a$ and modulating frequency $f_b$ can be expressed as:

$$f_a = \frac{U_\infty}{L} \cdot \frac{1}{M_\infty \left[1 + \frac{(\gamma-1)}{2} M_\infty^2\right]^{-1/2} + \frac{1}{K}} \tag{28}$$

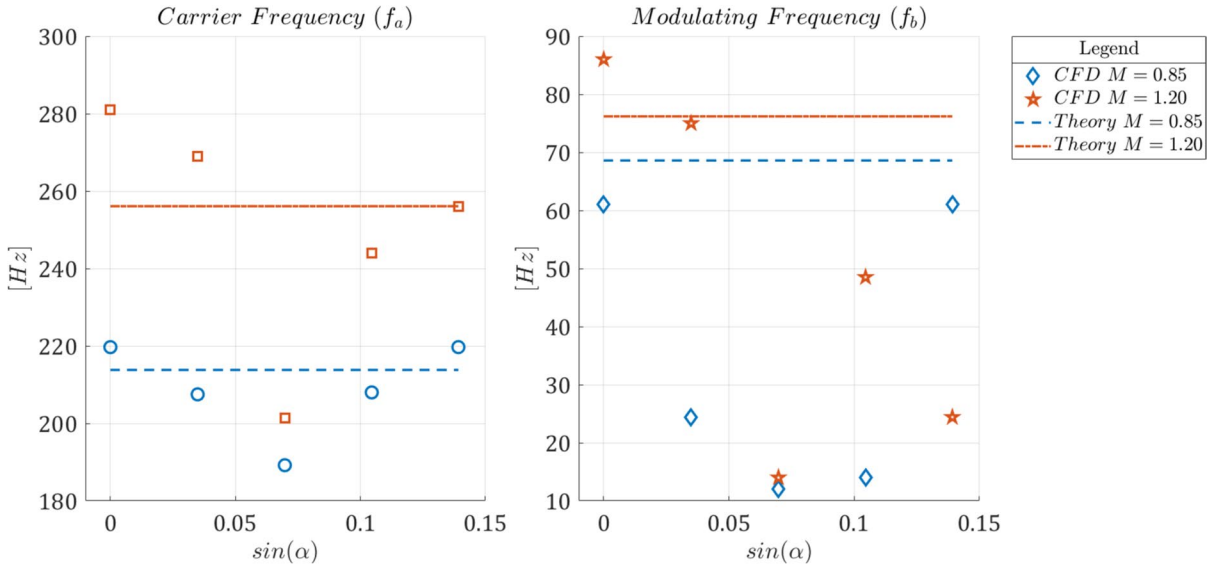


**Fig. 15** Variation of carrier and modulating frequencies (according to Delprat's decomposition) with angle of attack, and comparison with empirical calculated values

$$f_b = \frac{U_\infty}{D} \cdot \frac{0.062}{M_\infty \left[1 + \frac{(\gamma-1)}{2} M_\infty^2\right]^{-1/2} + \frac{1}{K}} \tag{29}$$

For the current case, the calculated values were $f_a$ 213.8 Hz and $f_b$ 68.6 Hz for Mach 0.85, and $f_a$ 256.1 Hz and $f_b$ 76.2 Hz for Mach 1.20. The comparison with CFD data is shown in Fig. 15

Here data is plotted against the sine of the angle of attack to show the effect of the velocity vector component directed towards the cavity, appearing with a positive angle of attack. At both Mach numbers, the variation of $f_a$ with an angle of attack was not linear. In both cases, the curves had a minimum at $\alpha = 4$. The trend of $f_b$ was even more irregular. At Mach 0.85, the modulating frequency value decreased with AoA up to $\alpha = 4$, did not appreciably change moving to $\alpha = 6$, and then increased again. At Mach 1.20, although the decrease observed up to $\alpha = 4$ was still present, with subsequent variation of incidence, $f_b$ increased at $\alpha = 6$ and then decreased again at $\alpha = 8$.

Previous studies (see for example [41–43]) developed correction values for the Rossiter-Heller equations, taking into consideration the flow topology and effective changes on the eddy convective speeds.[3] The reason was that, at least for open-type cavity flow, the internal main vortex shape (and hence length) changes with different flow conditions altering the cavity response. As shown in the "mean flow analysis", at both Mach numbers, angle of attack variations introduced changes in the topology of the eddies embedded inside the cavity, which in turn affected the flow resonating mechanism, and induced variations on the carrier and modulating frequencies. On the other hand, if this was the sole mechanism acting on the RH modes, a regular trend with an angle of attack should have been present instead of the irregularities observed in Fig. 15. It is possible, therefore, that other mechanisms (boundary layer thickness variations, changes in the vorticity shed from the separating shear layer, alterations of centrifugal instabilities of the main eddy) were affecting the flow and, with the nature of the RH modes extremely coupled and non-linear it was not possible, at this stage, to separate the effects. This would have been a separate activity on its own, which was outside the scope of the current study.

### 5.1.3 Acoustic Loads Distribution on Structures

To explore the acoustic load distribution on the cavity and door surfaces OASPL levels vs area distribution were plotted as shown in Fig. 16. Such analysis was deemed necessary for current and future aircraft designs. Knowledge of acoustic load distribution and extension is a design requirement for structural engineers to determine potential acoustic fatigue issues, especially in the presence of 3D printed structures and/or Radar Absorbing Materials/Coatings, which have a high susceptibility to acoustic fatigue. The OASPL level vs area distribution values were determined by calculating the area extension experiencing a determined range of OASPL values (for this study 20 levels were identified, ranging from

[3] The $K$ term of the empirical equation, which in the original Rossiter-Heller formulation is a constant.

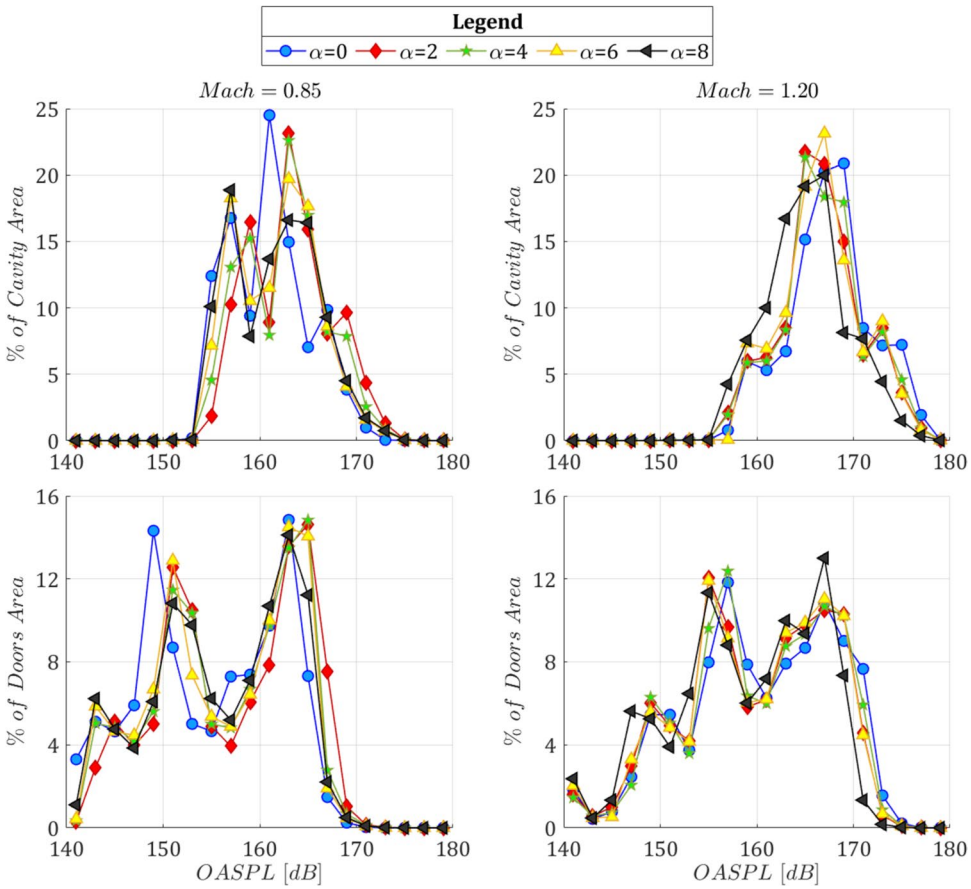


**Fig. 16** Acoustic load distribution for cavity (upper row) and doors (lower row) at different angles of attack. Left column, Mach 0.85. Right column, Mach 1.20

141 to 179 dB at intervals of 2 dB). The final area extension was then reported as the percentage of the total cavity (or doors) area. Hence, for example, a value of 24% at 161 dB for the cavity, indicated that 24% of the cavity area experienced OASPLs between 160 and 162 dB.

As shown in the top left of Fig. 16, at Mach 0.85 and zero angle of attack, the curve was characterised by two peaks, one at 161 dB and the other at 157 dB. The former comprised nearly a quarter of the cavity area, whilst for the latter, the value was 13%. Increasing the angle of attack, up to 4 deg, produced minimal change in the values of these two peaks but shifted their locations by 2 dB towards higher dB values. Further increases in the angle of attack reduced the higher dB-peak area to 20% at $\alpha = 6$ and to 12% at $\alpha = 8$. On the other hand, the second peak moved towards lower values and incorporated more surface of the cavity. From a quantitative point of view, at zero angle of attack 61% of the cavity surface experienced an OASPL above 160 dB. This value increased to 71% at $\alpha = 2$. Passed this point the cavity percentage area exposed to OASPL above 160 dB decreased, reaching the final value of 63% at $\alpha = 8$. This was consistent with the flow visualisation of Figs. 12 and 17, where a progressive increase of low-OASPL area (green-coloured) in the cavity's front part was observed. At Mach 1.2, the shape of the curve changed showing only a single dominant peak. In this case, the angle of attack effect was minimal, and the percentage of area exposed to OASPL of more than 160 dB remained at approximately 90%. Again, flow visualisation (Figs. 12, 13, and 17) indicated that OASPL inside the cavity was mainly independent of incidence. The overall picture was different when the doors were examined. The distribution curve (lower plots of Fig. 16) showed two distinct peaks at both Mach 0.85 and Mach 1.20, separated by an interval of more than 10 dB. This reflected the different acoustic loading of the door between the side exposed to the cavity flow (inner) and the side exposed to freestream flow (outer), as shown in Fig. 10. At Mach 0.85, the effect of angle of attack was observed on the door outer side-related peak, which moved to slightly higher OASPL values. On the other hand, the inner-side-related peak was not affected by incidence variations.

At Mach 1.20, the opposite was true, and in this case, it was the inner side of the door that experienced a marked increase in the percentage of area at $\alpha = 8$. Regarding the percentage of the door surface exposed to OASPL levels more than 160 dB, the figures indicated that at Mach 0.85 and $\alpha = 0$, the corresponding value was 34%. Upon increasing incidence, this increased up to 45% at $\alpha = 2$,

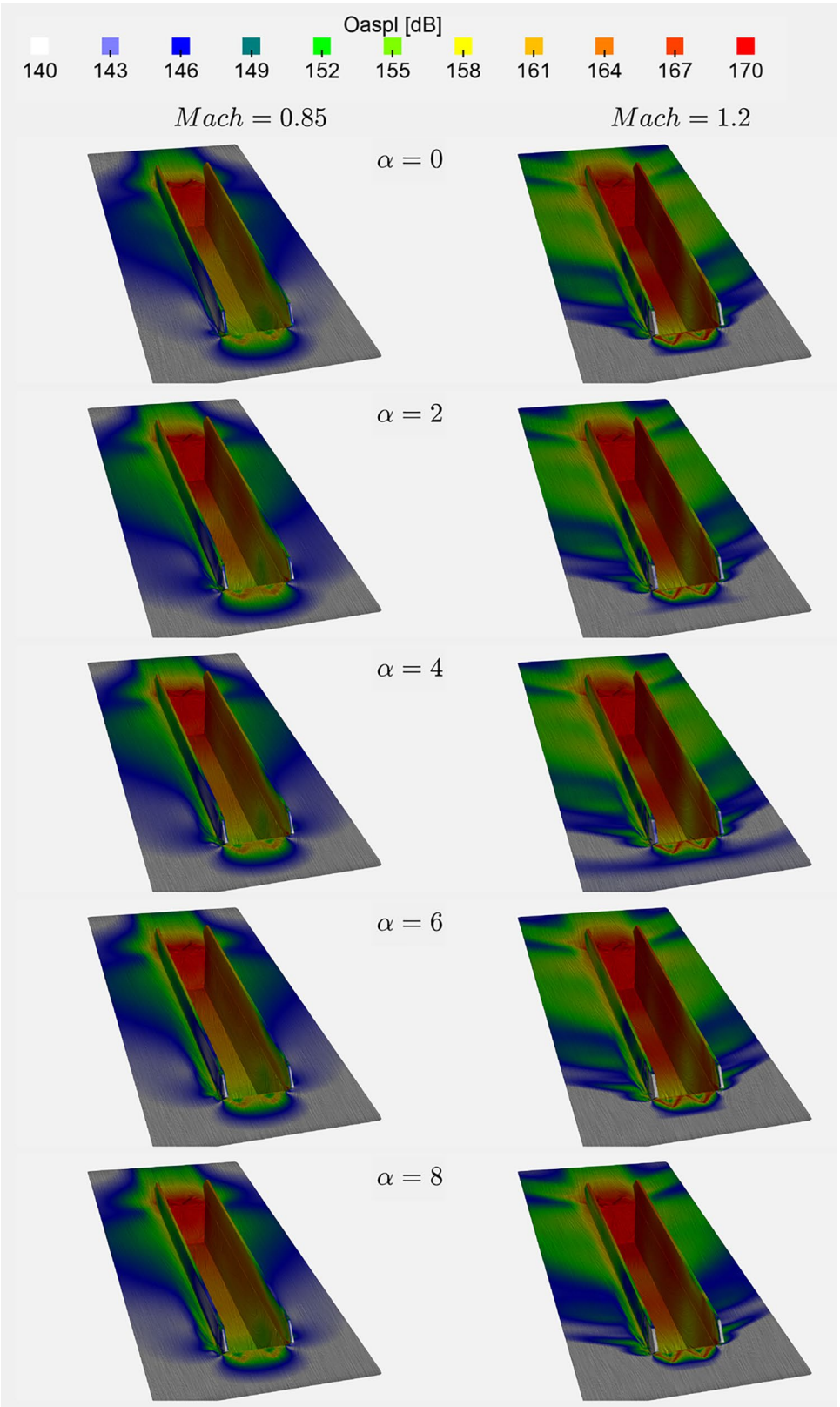


**Fig. 17** Comparison of mean wall-shear LIC coloured by OASPL. Left column, angle of attack sweep at Mach 0.85. Right column, angle of attack sweep at Mach 1.20

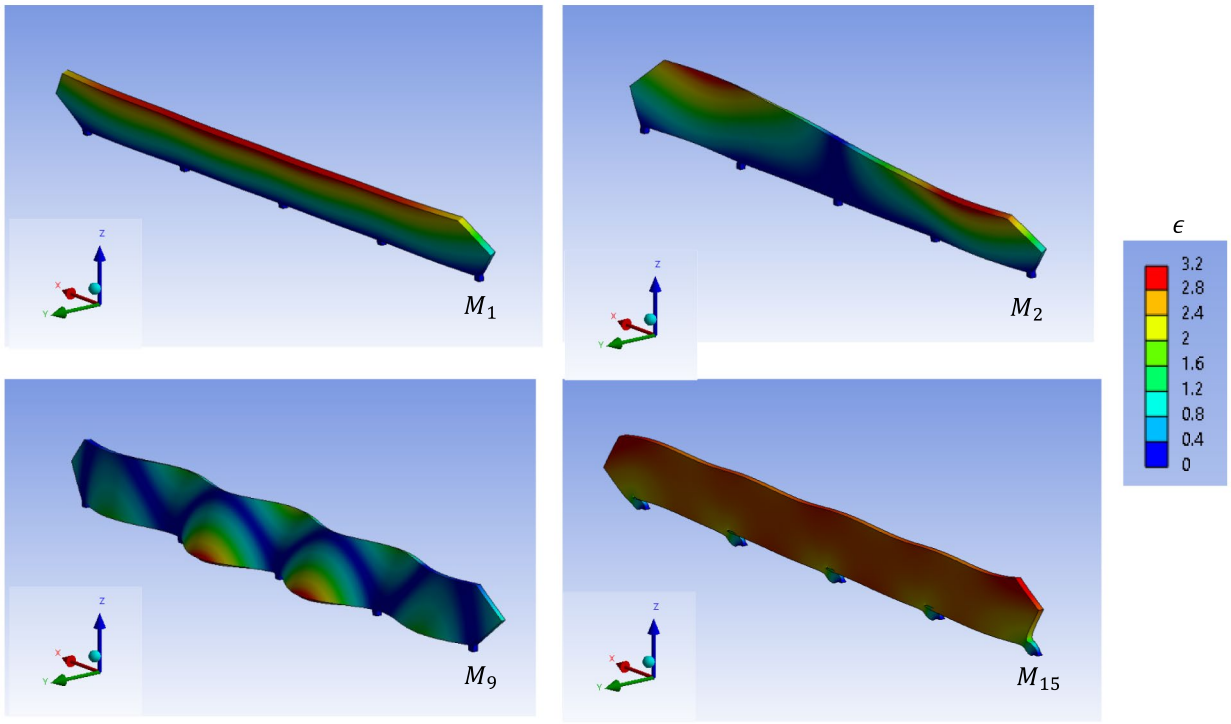


**Fig. 18** Principal structural modes visual identification. Contours coloured by non-dimensional deformation (ratio of local nodal displacement to maximum nodal displacement)

and then remained constant upon further increases in angle of attack. At Mach 1.20, 52% of the door area experienced OASPL values above 160 dB, and no variations on this value were observed upon increasing incidence.

## 5.2 Modal Analysis

A total of 20 modes were extracted during the structural analysis. Nevertheless, just four were considered fundamental, as they accounted for more than 75% of the effective total mass in all principal directions of deformation. These were $M_1$ (385 Hz), $M_2$(487 Hz), $M_9$(1840 Hz), and $M_{15}$ (3885 Hz). The associated displacements are shown in Fig. 18.

$M_1$ comprised a flexural response along the door's y-axis coupled with torsional deformation along the x-axis and z-axis. $M_2$ was related to the torsional deformation of the structure in the z-axis. The difference between $M_1$ and $M_2$, regarding the deformation around the z-axis, was that $M_2$ had a nodal point whilst $M_1$ did not. $M_9$, still involved a flexural response along the y-axis, but differed from $M_1$ as the former contained multiple nodal points, coincident with the hinges. Finally, $M_{15}$ represented shear deformation along the x-axis. Table 4 summarises these principal modes with their relative contribution to the total mass for each direction. It was noteworthy that no appreciable contribution was observed for $u_z$ and $\theta_y$. This outcome was, nevertheless, expected as these deformation directions were directly blocked by the no displacement constraint imposed on the base of the hinges.

**Table 4** Summary of principal mode characteristics for the hinged door

| Mode | $f$[Hz] | Ratio of effective mass to total mass % | | | | | |
|---|---|---|---|---|---|---|---|
| | | $u_x$ | $u_y$ | $u_z$ | $\theta_x$ | $\theta_y$ | $\theta_z$ |
| $M_1$ | 385 | – | 75.05 | – | 99.11 | – | 54.86 |
| $M_2$ | 487 | – | – | – | – | – | 20.25 |
| $M_9$ | 1840 | – | 10.62 | – | – | – | – |
| $M_{15}$ | 3885 | 98.87 | – | – | – | – | – |
| Total | | 98.87 | 85.67 | - | – | – | – |

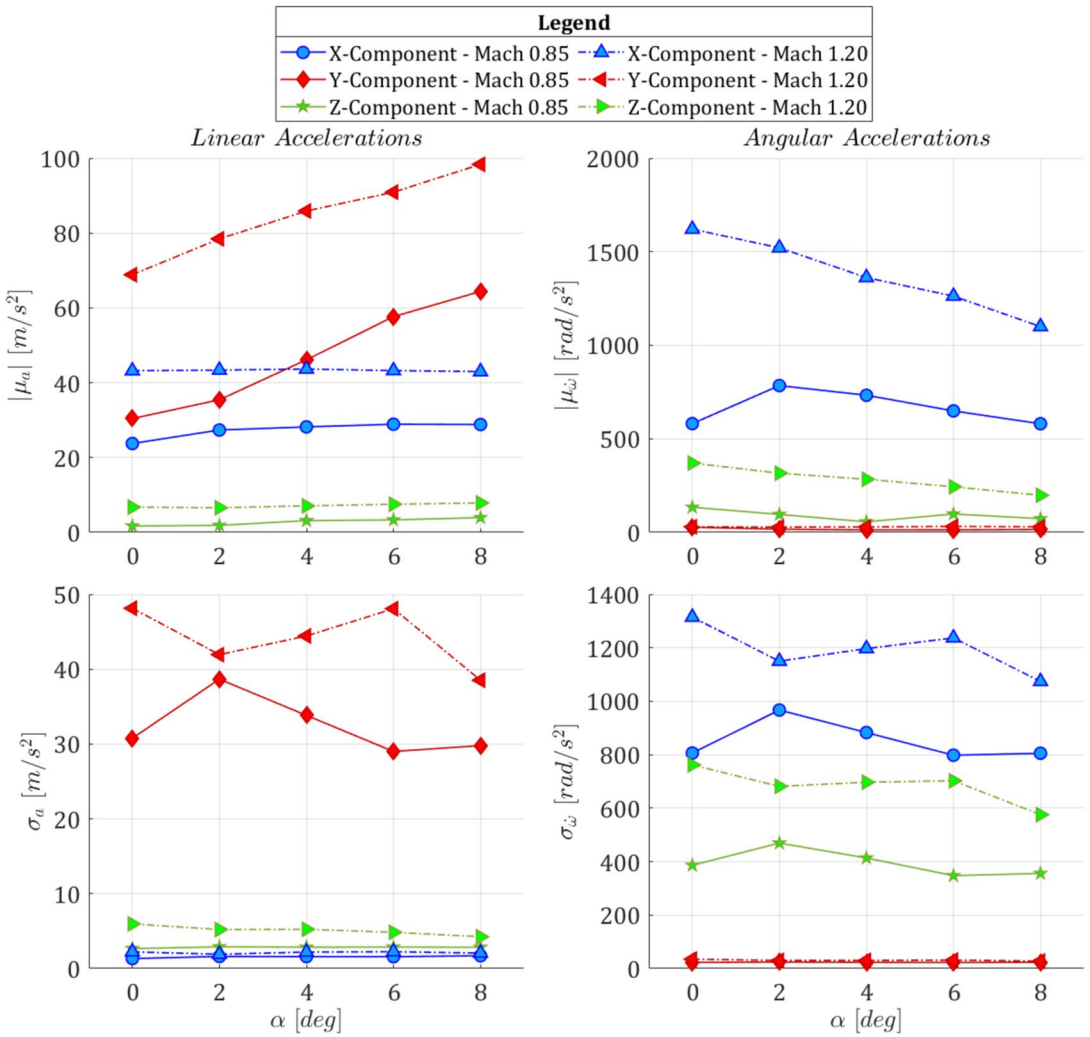


**Fig. 19** Angle of attack effects on mean and RMS absolute values of angular and linear acceleration components relative to bay doors

## 5.3 Door Load Analysis

Door effects were reported in terms of linear and angular accelerations. Again, the analysis was divided between mean values (and the relative RMS trends) and the associated spectra.

Analysis of the mean values of linear accelerations indicated a predominance in the y-direction (Fig. 19-Upper left). At Mach 0.85, the x-component and the y-component were similar, but at Mach 1.20 this was not the case, with $\mu_{a_y}$ attaining a value twice as big as $\mu_{a_x}$. On the other hand, the linear acceleration along the z-direction was an order of magnitude smaller than the other components at both velocities. Angle of attack influence was only observed on the y-component which linearly increased at both Mach numbers. By contrast, the incidence did not affect the x and z components. The analysis of the RMS values (Fig. 19-Lower left) showed a strong unsteadiness in time of the y-component. In this case, the angle of attack influence was negligible.

Regarding angular accelerations, the x component was dominant for both mean and RMS values (-Upper and lower right). The z-component was the second in order of magnitude and attained high RMS values as well. The overall effect of incidence was to decrease the magnitude of both mean and RMS values. These findings indicated that the main effect of the flow was a tendency to push the doors open or closed, whilst the drag effect along the flow direction was of a secondary order.

Spectral analysis of accelerations was separated by components and is summarised in Figs. 20, 21, and 22. In the x-direction, the critical frequencies were represented by $M_1$

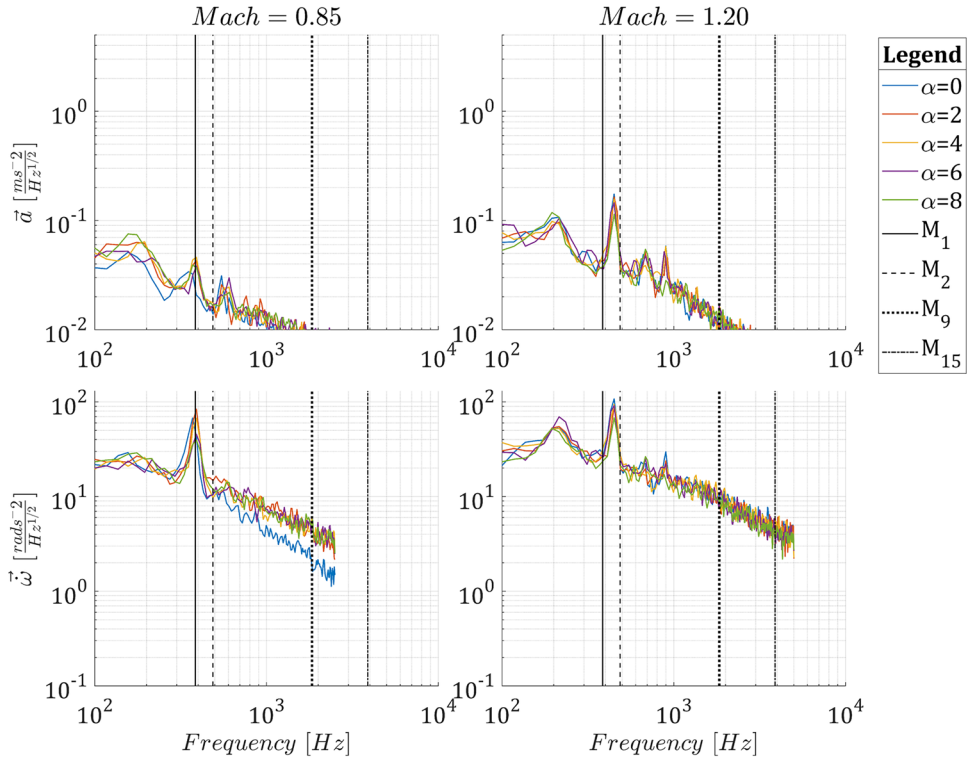


**Fig. 20** Angle of attack effects on spectra of angular and linear accelerations relative to bay doors. X-component

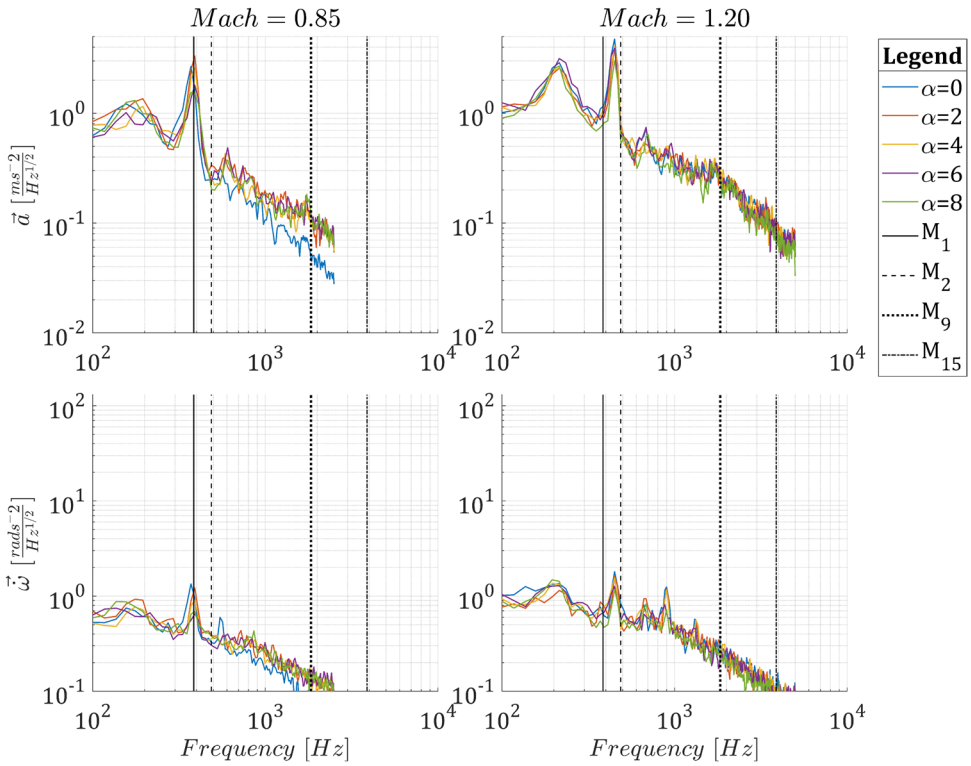


**Fig. 21** Angle of attack effects on spectra of angular and linear accelerations relative to bay doors. Y-component

(385 Hz) and $M_{15}$ (3885 Hz), accounting for 99% of the participation factor, respectively for rotation and translation. At Mach 0.85, the spectrum of x-linear accelerations (Fig. 20-Upper) showed low-power spectra, with resonant peaks located in the band between 150 and 900 Hz, away

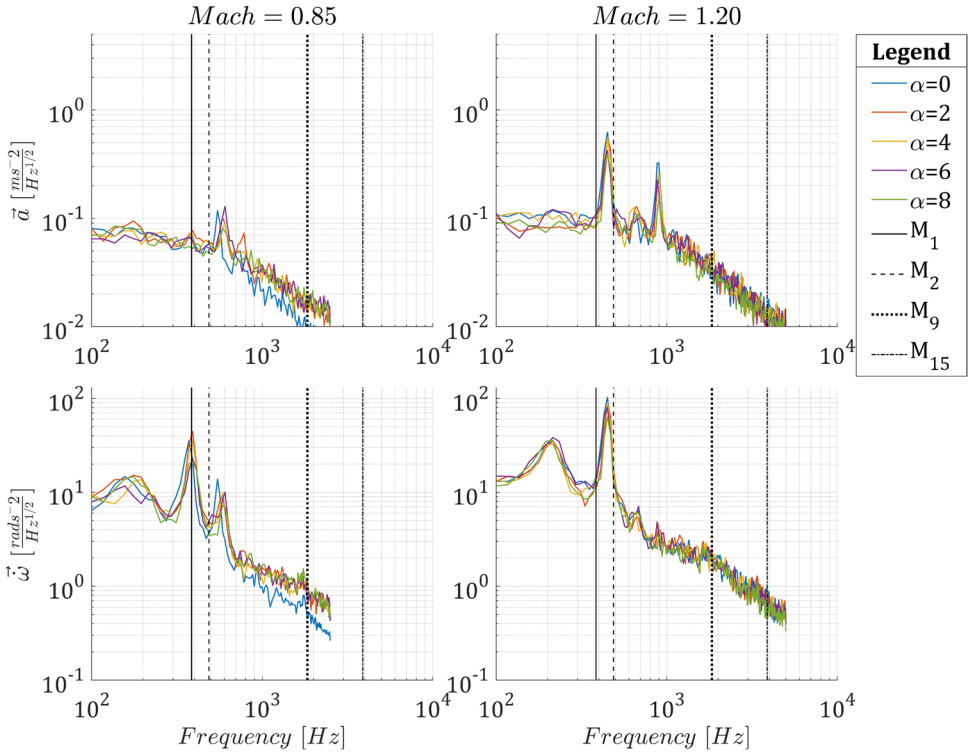


**Fig. 22** Angle of attack effects on spectra of angular and linear accelerations relative to bay doors. Z-component

from the critical value of $M_{15}$, hence not constituting potential problems in terms of fluid–structure interaction.

By contrast, the spectrum of angular accelerations at Mach 0.85 (Fig. 20-Lower left), showed the presence of a high power peak, corresponding with the critical frequency $M_1$. If the speed was increased to Mach 1.20, the main peak moved to higher frequencies (~450 Hz), and a secondary tone appeared centred at 215 Hz. The overall effect of the angle of attack was different between the two Mach numbers. At Mach 0.85, for $\alpha = 2$, there was an increase in the overall power of 30%, compared to the zero incidence case. However, further increasing incidence, progressively reduced it, with a final power, at $\alpha = 8$, 40% lower than $\alpha = 0$. This trend closely reflected that of the pressure signals discussed in the previous section. At Mach 1.20, the main peak experienced a constant decrease in power with angle of attack, whilst the second one remained nearly unaffected except for the $\alpha = 6$ case, which represented the highest value attained by this tone.

In the y-component analysis, the key modes were $M_1$ (385 Hz) and $M_9$(1840 Hz). Here the response of angular acceleration (Fig. 21-Lower) attained power levels an order of magnitude smaller than the x-component and z-component and hence was considered negligible. On the other hand, the linear acceleration in the y-direction was the most prominent. Fourier analysis (Fig. 21-Upper) showed that at Mach 0.85 a peak was present, corresponding to$M_1$. This was accompanied by a secondary one at 195 Hz. Similar, to the x-component case, the trend with angle of attack was an initial increment in power up to $\alpha = 2$, followed by a constant decrease moving to higher incidences. At Mach 1.20 the main peak moved toward higher frequencies (~450 Hz), whilst the second one appeared, centred at 214 Hz, having a power similar to the dominant tone .

Finally, the z-direction modes were related to $M_1$ (385 Hz) and $M_2$(487 Hz) accounting for 55% and 20% of the rotation around this direction respectively. The door linear acceleration spectra (Fig. 22-Upper) were of low power in the Mach 0.85 case, but at Mach 1.20 two high-power peaks appeared at 450 Hz and 898 Hz. Nevertheless, these were considered of secondary importance as the doors did not present displacement modes in the z-direction. Conversely, angular accelerations indicated that potential fluid–structure interactions were likely to occur at both Mach numbers (Fig. 22-Lower). At Mach 0.85, a major peak was again observed corresponding to $M_1$, with a secondary one relatively close to $M_2$ at 550 Hz. At Mach 1.20 the major tone occurred at 450 Hz, indicating a potential coupling with $M_2$. As in the case of the x and y components, in this Mach regime, a second peak was present at 214 Hz.

The overall analysis of the spectral signature on linear and angular accelerations acting on the doors indicated that the possibility of fluid-acoustic coupling was likely to occur as all spectra showed a predominant tone located at the same frequency as the first structural mode $M_1$. This mode was characterised by having almost entirely

the structure effective mass for displacements along the y-direction, and rotations around the x and z-axes. As linear acceleration was dominated by the $a_y$ component and angular acceleration by the $\dot{\omega}_x$ and $\dot{\omega}_z$ components, aerodynamic-induced structural resonance was likely to occur.

### 5.4 Correlation Between Pressure and Acceleration Signals

The final part of the analysis concentrated on exploring correlations between pressure fluctuations on the cavity floor and accelerations experienced by the doors. As shown in previous sections there was a strong influence on the linear and angular acceleration generated by the cavity's main resonant modes. The coherence between the pressure

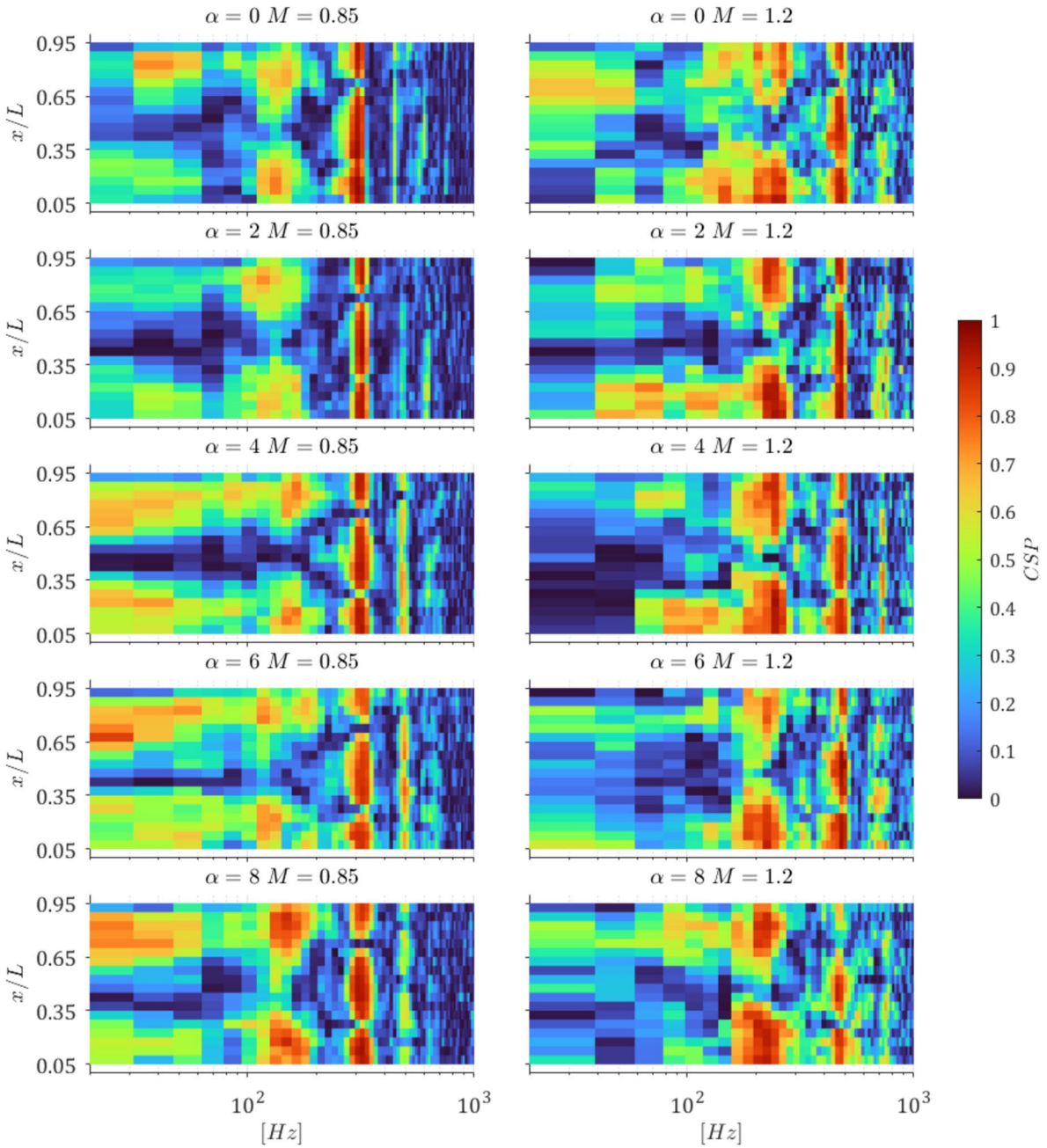


**Fig. 23** Comparison cross-spectrum between pressure signal and door's linear acceleration magnitude. Left column, angle of attack sweep at Mach 0.85. Right column, angle of attack sweep at Mach 1.20

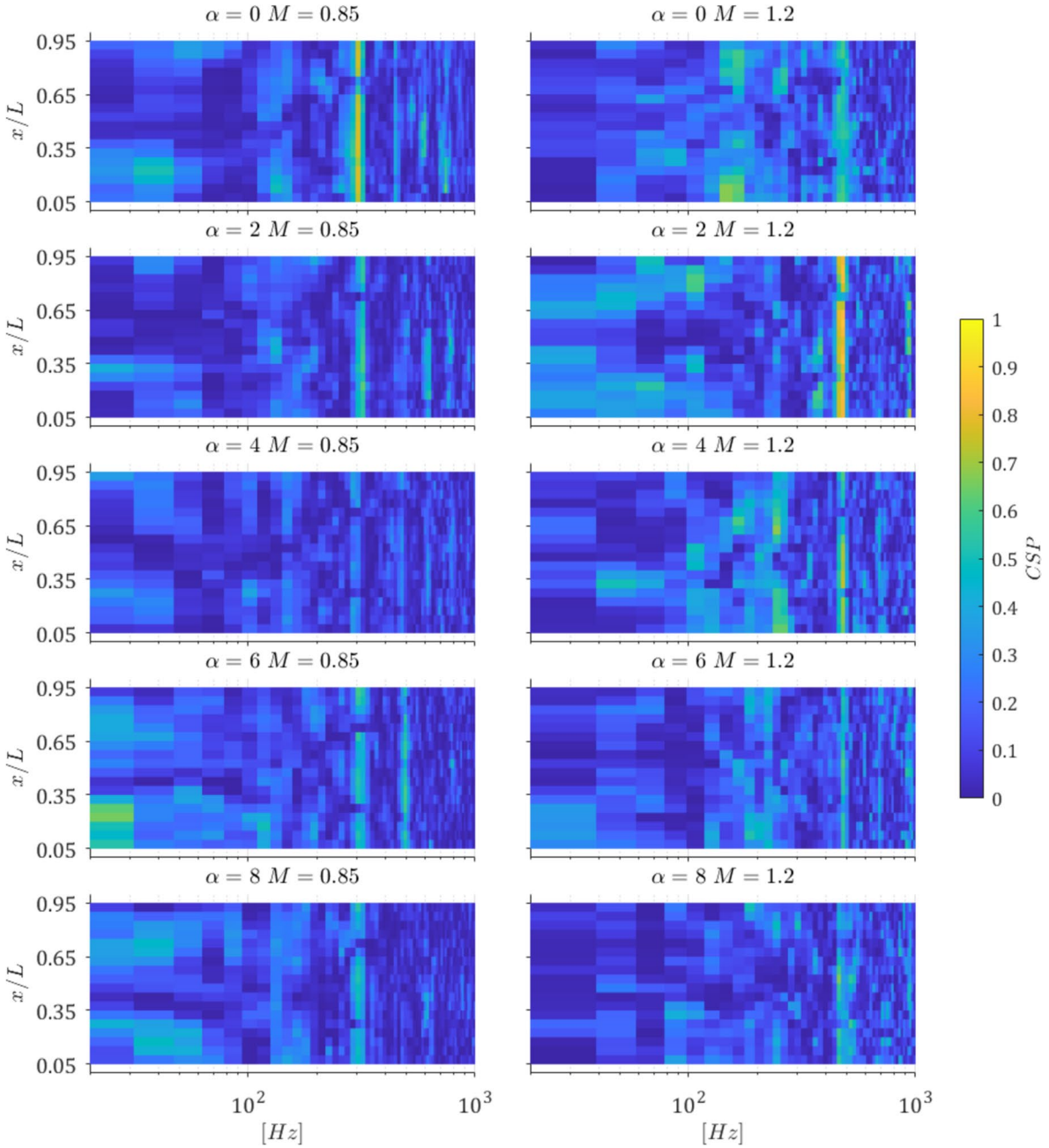


**Fig. 24** Comparison cross-spectrum between pressure signal and door's angular acceleration magnitude. Left column, angle of attack sweep at Mach 0.85. Right column, angle of attack sweep at Mach 1.20

signals recorded along the cavity central rake and the magnitude of linear and angular accelerations was therefore explored. It was preferred to focus on the coherence instead of the coherent output power, as the latter, although being a direct indicator of output-to-input power response, would have been dominated by the 2nd Rossiter-Heller mode as being the dominant tone since its power was the order of magnitudes above the other resonating modes and the background noise. On the other hand, this section aimed to determine how the angle of attack affected the relative correlation of the different modes on the door's imposed accelerations.

The results for each Mach number/angle of attack combination are shown in Figs. 23 and 24. Each of these contours reports the spectral coherence between the acceleration signal experienced by the doors and the pressure signal monitored at different longitudinal stations.

At Mach 0.85 (Fig. 23-left column) the highest coherence for linear acceleration, with values of 0.9, was observed at a frequency of 378 Hz, which corresponded to $R_2$. The shape along the cavity length (vertical slice) assumed the classical W-pattern, agreeing with the findings of previous studies that examined how the intensity of this mode varied along the bay [4]. The result confirmed that the strongest acoustic mode exercised the highest energy transfer from flow to doors (the strongest linear accelerations). In the CSP map there were also areas where $R_1$ (159 Hz) and $R_3$ (549 Hz) coupled with the doors' linear accelerations, with CSP values of 0.6 and 0.4 respectively. Upon increasing the angle of attack only minor variations were observed with $R_2$, which still had the highest coherence. By comparison the band of $R_3$ increased its coherence value, achieving 0.5 at $\alpha = 2, 0.73$ at $\alpha = 4, 0.75$ at $\alpha = 6$, and 0.58 at $\alpha = 8$. The trend reflected the variation in power experienced by this mode upon varying the incidence (see Fig. 14). Similarly, $R_1$ coherence changed with the angle of attack achieving a maximum of 0.88 at $\alpha = 8$, and a minimum of 0.6 at zero incidence.

At Mach 1.2 (Fig. 23-right column) $R_1$(band at 244 Hz) became highly relevant, achieving coherence values above 0.9. This occurred with $R_2$ (band at 476 Hz) maintaining its high relevance similarly to the Mach 0.85 case. On the other hand, $R_3$ coherence was barely observable at zero AoA, though it became relevant at higher incidences following its emergence from the background noise as shown by the SPL analysis. All modes assumed, in the streamwise direction, patterns already observed in previous studies [4]. For $R_1$ the classical V-shape (two peaks and one dip) was observed, whilst $R_2$ assumed a W-shape pattern (three peaks and two dips). Finally, $R_3$ was characterised by four peaks and three dips.

The situation for the angular accelerations was different when compared to the linear ones. For the Mach 0.85 case (Fig. 24-left column) only $R_2$ achieved a coherence greater than 0.8, whilst all other resonant modes did not present a correlation with the door's angular acceleration. The picture remained unchanged if the incidence was raised to 2 deg, although the maximum coherence value in this case was 0.6. On increasing the incidence, no appreciable correlation between the angular acceleration vector and the pressure signals was observed.

For the Mach 1.2 case (Fig. 24-right column) again, only $R_2$ achieved a relevant CSP value (0.5 at $\alpha = 0$). The maximum was observed at $\alpha = 2$, with a value of 0.85. Nevertheless, further increases in the angle of attack lowered the coherence value observed for $R_2$, being practically non-existent at $\alpha = 6$ and $\alpha = 8$. This was similar to the trend observed for the intensity of $\vec{\omega}$, which decreased upon increasing the angle of attack (see Fig. 19) and the fact that $R_2$, continuously reduced the power upon an increase in the angle of attack past its peak value achieved at $\alpha = 2$.

## 6 Conclusion

The study explored the influence of the angle of attack, in the acoustic response and the induced forces on the doors related to a representative model of a low-RCS weapon bay at Mach 0.85 and 1.20.

The overall incidence effect varied according to the speed regime at which the cavity was exposed. At Mach 0.85, a critical value for the angle of attack, between 0 and 4 deg, was shown to exist, up to which the OASPL and SPL response of cavity the increased. Beyond this angle of attack, the acoustic response decreased with incidence. Flow analysis indicated that the angle of attack correlated with boundary layer thickness at the cavity edge and with a minor change in position and configuration of the cavity's main recirculatory vortex.

At Mach 1.20, this trend was confirmed qualitatively, but the effects were minor, and in some parts of the cavity, OASPL values did not change with incidence variations. Inspection of the OASPL contours showed that the main effect of the angle of attack on the flow configuration was on the bay's leading shock wave, which changed in shape even with minor variations in incidence. The overall conclusion was that the acoustic response of the cavity was mainly dependent on Mach number. Incidence variations induced local flow modifications which altered the cavity acoustic response, especially in the frequency domain.

The analysis of disturbances induced by the flow on the door structure indicated that the major contribution was correlated with the linear acceleration in the y-direction and angular accelerations in the x and z-directions. Angle of attack variations had secondary importance in the unsteady part of the accelerations. Here modal analysis indicated that fluid–structure resonance was possible, as the main door mode coincided with the strongest peak in the acceleration spectra.

On the other hand, it was observed that the most prominent influence of angle of attack for this study was observed in the analysis of the mean values of the strongest components of acceleration, which were in the y-direction for the linear case, and in the x-direction for the angular case. The former nearly increased by 100% moving from $\alpha = 0$ to $\alpha = 8$ at both Mach numbers. Instead, the mean value for the x-component of angular acceleration, whilst being nearly insensitive to incidence variations at Mach 0.85, decreased by up to 25% at Mach 1.20 when the angle of attack was increased to 8 deg.

The coherence spectral anlaysis demonstrated that the dominant modes appearing in the acoustic spectrum were directly correlated to linear and angular acceleration spectra, which in turn indicated that these acoustic modes

were the major cause of excitations induced by the flow on weapons bay doors.

**Author Contributions** D.B. performed CFD analysis and numerical postprocessing. A.J.S. performed the analysis of CFD data. All authors reviewed the manuscript

**Data Availability** No datasets were generated or analysed during the current study.

## Declarations

**Conflict of interest** The authors declare no competing interests.



## References

1. Rockwell, D., Naudascher, E.: Review—self-sustaining oscillations of flow past cavities. J. Fluids Eng. **100**(2), 152–165 (1978). https://doi.org/10.1115/1.3448624
2. Rossiter, J.E., Royal A.E.R.: Wind tunnel experiments on the flow over rectangular cavities at subsonic and transonic speeds, London. (1964).
3. Heller, H.H., Holmes, D.G., Covert, E.E.: Flow-induced pressure oscillations in shallow cavities. J. Sound Vib.Vib. **18**(4), 545–553 (1971). https://doi.org/10.1016/0022-460X(71)90105-2
4. Tracy, M.B., Plentovich, E.B.: Cavity unsteady-pressure measurements at subsonic and transonic speeds. NASA Technical Paper. (1997).
5. Kannepalli, C., Chartrand, C., Birkbeck, R., Sinha, N., Murray, N.: Computational modeling of geometrically complex weapons bays. In: 17th AIAA/CEAS Aeroacoustics Conference (32nd AIAA Aeroacoustics Conference), American Institute of Aeronautics and Astronautics. (2011). https://doi.org/10.2514/6.2011-2774
6. Ukeiley, L., Sheehan, M., Coiffet, F., Alvi, F., Arunajatesan, S., Jansen, B.: Control of pressure loads in geometrically complex cavities. J. Fluid Mech. (2008). https://doi.org/10.2514/1.33324
7. Barone, M.F., Arunajatesan, S.: A computational study of flow within cavities with complex geometric features. 53rd AIAA Aerospace Sciences Meeting, American Institute of Aeronautics and Astronautics. (2015). https://doi.org/10.2514/6.2015-0008
8. Casper, K.M., Wagner, J.L., Beresh, S.J., Henfling, J., Spillers, R., Pruett, B. O.: Complex geometry effects on open cavity dynamics. 32nd AIAA Applied Aerodynamics Conference, American Institute of Aeronautics and Astronautics. (2014). https://doi.org/10.2514/6.2014-3025
9. Casper, K.M., Wagner, J.L., Beresh, S.J., Spillers, R., Henfling, J.: Unsteady pressure sensitive paint measurements of resonance properties in complex cavities. In: 46th AIAA Fluid Dynamics Conference, American Institute of Aeronautics and Astronautics. (2016). https://doi.org/10.2514/6.2016-3315
10. Lawson, S.J., Barakos, G.N.: Computational fluid dynamics analyses of flow over weapons-bay geometries. J. Aircr.Aircr. **47**(5), 1605–1623 (2010). https://doi.org/10.2514/1.C000218
11. Kannepalli, C., Chartrand, C., Birkbeck, R., Sinha, N., Murray, N.: Computational modeling of geometrically complex weapons bays. In: AIAA 2011-2774. 17th AIAA/CEAS Aeroacoustics Conference (32nd AIAA Aeroacoustics Conference) (2011)
12. Shaw, L.L.: Suppression of aerodynamically induced cavity pressure oscillations. J. Acoust. Soc. Am.Acoust. Soc. Am. (1979). https://doi.org/10.1121/1.383242
13. Sheta, E.F., Harris, R.E., Luke, E.A., George, B., Ukeiley, L.S.: Loads and acoustics prediction on deployed weapons bay doors. In: 33rd AIAA Applied Aerodynamics Conference, American Institute of Aeronautics and Astronautics. (2015). https://doi.org/10.2514/6.2015-3018
14. Daumas, L., Chalot, F., Levasseur, V., Mallet, M., Reau, N.: LES and DES aeroacoustic simulations for inflght opened Weapon Bay. (2009).
15. Blair, A.B., Stallings, R.L.: Cavity door effects on aerodynamic loads of stores separating from cavities. J. Aircr.Aircr. **26**(7), 615–620 (1989). https://doi.org/10.2514/3.45811
16. Mancini, S., Kolb, A., Mayer, F.: Reducing aeroacoustic feedback mechanisms in rectangular cavity flows using passive modifications, AIAA AVIATION 2021 FORUM, American Institute of Aeronautics and Astronautics. (2021). https://doi.org/10.2514/6.2021-2126
17. Bacci, D., Saddington, A.J., Bray, D.: The effect of angle of attack on the aeroacoustic environment within the weapons bay of a generic UCAV. Aerosp. Sci. Technol.. Sci. Technol. **93**, 105315 (2019). https://doi.org/10.1016/j.ast.2019.105315
18. Loupy, G.J.M., Barakos, G.N., Taylor, N.J.: Cavity flow over a transonic weapons bay during door operation. J. Aircr.Aircr. **55**(1), 339–354 (2017). https://doi.org/10.2514/1.C034344
19. Menter, F.R., Egorov, Y.: The scale-adaptive simulation method for unsteady turbulent flow predictions. Part 1: theory and model description. Flow Turbul. Combust.Turbul. Combust. **85**(1), 113–138 (2010). https://doi.org/10.1007/s10494-010-9264-5
20. Egorov, Y., Menter, F.R., Lechner, R., Cokljat, D.: The scale-adaptive simulation method for unsteady turbulent flow predictions. Part 2: application to complex flows. Flow Turbul. Combust.Turbul. Combust. (2010). https://doi.org/10.1007/s10494-010-9265-4
21. Menter, F.R.: Two-equation Eddy-viscosity turbulence models for engineering applications. AIAA J. **32**(8), 1598–1605 (1994). https://doi.org/10.2514/3.12149
22. Majumdar, S.: Role of underrelaxation in momentum interpolation for calculation of flow with nonstaggered grids. Numer. Heat Transfer **13**(1), 125–132 (1988)
23. Rhie, C.M., Chow, W.L.: Numerical study of the turbulent flow past an airfoil with trailing edge separation. AIAA J. **21**(11), 1525–1532 (1983). https://doi.org/10.2514/3.8284
24. Barth, T., Jespersen, D.: The design and application of upwind schemes on unstructured meshes, 27th Aerospace Sciences Meeting. https://doi.org/10.2514/6.1989-366
25. Leonard, B.P.: The ULTIMATE conservative difference scheme applied to unsteady one-dimensional advection. Comput. Methods Appl. Mech. Eng.. Methods Appl. Mech. Eng. **88**(1), 17–74 (1991). https://doi.org/10.1016/0045-7825(91)90232-U
26. Menter, F. R.: Best practice: scale-resolving simulations in ANSYS CFD, Ver. 2.00. (2015). https://doi.org/10.1155/2013/859465
27. Chaplin, R., Birch, T.: The aero-acoustic environment within the weapons bay of a generic ucaV. 30th AIAA Applied

Aerodynamics Conference, American Institute of Aeronautics and Astronautics. (2012). https://doi.org/10.2514/6.2012-3338
28. Henshaw, M.J.D.C.: M219 cavity case: verification and validation data for computational unsteady aerodynamics. Tech. Rep. RTO-TR-26, AC/323(AVT)TP/19. (2002).
29. Celik, I.B., Cehreli, Z.N., Yavuz, I.: Index of resolution quality for large eddy simulations. J. Fluids Eng. **127**(5), 949–958 (2005). https://doi.org/10.1115/1.1990201
30. Rajkumar, K., Tangermann, E., Klein, M.: Efficient scale-resolving simulations of open cavity flows for straight and sideslip conditions. Fluids (2023). https://doi.org/10.3390/fluids8080227
31. Clough, R.W., Penzien, J.: Dynamics of structures. Mc-Graw-Hill, New York, USA (1975)
32. Welch, P.D.: The use of fast Fourier transform for the estimation of power spectra: a method based on time averaging over short, modified periodograms. IEEE Trans. Audio Electroacoust.Electroacoust. (1967). https://doi.org/10.1109/TAU.1967.1161901
33. Thangamani, V., Knowles, K., Saddington, A.J.: Effects of scaling on high subsonic cavity flow oscillations and control. J. Aircr. Aircr. **51**(2), 424–433 (2014). https://doi.org/10.2514/1.C032032
34. Mathias, M.S., Medeiros, M.A.F.: The effect of incoming boundary layer thickness and mach number on linear and nonlinear rossiter modes in open cavity flows. Theoret. Comput. Fluid Dyn.. Comput. Fluid Dyn. **35**(4), 495–513 (2021). https://doi.org/10.1007/s00162-021-00570-2
35. Knowles, R.D., Finnis, M.V., Saddington, A.J., Knowles, K.: Planar visualization of vortical flows. P. I. Mech. Eng. G–J. Aer. **220**(G6), 619–627 (2006). https://doi.org/10.1243/09544100JAERO75
36. Bacci, D.: Transonic aero-acoustic of weapons bay, Cranfield University/Defence Academy of the United Kingdom. (2017).
37. Murray, N., Jansen, B., Rich, D.: Effect of door configuration on cavity flow modulation process. In: 17th AIAA/CEAS Aeroacoustics Conference (32nd AIAA Aeroacoustics Conference), American Institute of Aeronautics and Astronautics. (2011). https://doi.org/10.2514/6.2011-2773
38. Bacci, D., Saddington, A.J., Bray, D.: Identification of the formation of resonant tones in compressible cavity flows. Aerosp. Sci. Technol.. Sci. Technol. (2018). https://doi.org/10.1016/j.ast.2018.03.013
39. Basley, J., Pastur, L.R., Lusseyran, F., Soria, J., Delprat, N.: On the modulating effect of three-dimensional instabilities in open cavity flows. J. Fluid Mech. (2014). https://doi.org/10.1017/jfm.2014.576
40. Delprat, N.: Low-frequency components and modulation processes in compressible cavity flows. J. Sound Vib.Vib. (2010). https://doi.org/10.1016/j.jsv.2010.05.013
41. Gabel, M., Sarigul-Klijn, N.: The Rossiter equation: improving the fractional vortex speed and defining an effective length to depth ratio for cavity flows. The J. Acoust. Soc. Am. **155**(2), 952–961 (2024). https://doi.org/10.1121/10.0024722
42. Casalino, D., Gonzalez-Martino, I., Mancini, S.: On the Rossiter-Heller frequency of resonant cavities. Aerosp. Sci. Technol.. Sci. Technol. **131**, 108013 (2022). https://doi.org/10.1016/j.ast.2022.108013
43. DeChant, L.: A cavity depth sensitized rossiter mode formula. Appl. Math. Comput.Comput. **347**, 143–148 (2019). https://doi.org/10.1016/j.amc.2018.10.048